

RESEARCH ARTICLE

10.1029/2021JD036253

Key Points:

- The frequency of episodic dust events was higher during ATOMIC than normal for the Caribbean in January and February
- Relative amounts of dust and biomass burning aerosol were modulated by the location of the North Atlantic subtropical high
- Cloud Condensation Nuclei concentrations were highest when dust was mixed with biomass

Correspondence to:

P. K. Quinn,
patricia.k.quinn@noaa.gov

Citation:

Quinn, P. K., Bates, T. S., Coffman, D. J., Upchurch, L. M., Johnson, J. E., Brewer, A., et al. (2022). Wintertime observations of tropical Northwest Atlantic aerosol properties during ATOMIC: Varying mixtures of dust and biomass burning. *Journal of Geophysical Research: Atmospheres*, 127, e2021JD036253. <https://doi.org/10.1029/2021JD036253>

Received 23 NOV 2021

Accepted 19 MAR 2022



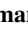

Author Contributions:

Conceptualization: P. K. Quinn, P. Zuidema
Data curation: T. S. Bates
Formal analysis: P. K. Quinn, T. S. Bates, A. Brewer, S. Baidar, I. L. McCoy, P. Zuidema
Funding acquisition: P. K. Quinn
Investigation: P. K. Quinn, T. S. Bates, L. M. Upchurch, J. E. Johnson, A. Brewer, S. Baidar
Methodology: P. K. Quinn
Project Administration: P. K. Quinn
Software: T. S. Bates, J. E. Johnson
Supervision: P. K. Quinn

© 2022. The Authors. This article has been contributed to by U.S. Government employees and their work is in the public domain in the USA.

This is an open access article under the terms of the [Creative Commons Attribution-NonCommercial-NoDerivs License](https://creativecommons.org/licenses/by/4.0/), which permits use and distribution in any medium, provided the original work is properly cited, the use is non-commercial and no modifications or adaptations are made.

Wintertime Observations of Tropical Northwest Atlantic Aerosol Properties During ATOMIC: Varying Mixtures of Dust and Biomass Burning

P. K. Quinn¹ , T. S. Bates^{1,2} , D. J. Coffman¹, L. M. Upchurch^{1,2}, J. E. Johnson^{1,2}, A. Brewer³, S. Baidar^{3,4}, I. L. McCoy^{5,6} , and P. Zuidema⁶ 

¹NOAA PMEL, Seattle, WA, USA, ²CICOES, University of Washington, Seattle, WA, USA, ³NOAA CSL, Boulder, CO, USA, ⁴CIRES, University of Colorado, Boulder, CO, USA, ⁵UCAR, Boulder, CO, USA, ⁶Department of Atmospheric Sciences, Rosenstiel School, University of Miami, Miami, FL, USA

Abstract The Atlantic Tradewind Ocean-Atmosphere Mesoscale Campaign (ATOMIC) took place from 7 January to 11 July 2020 in the tropical North Atlantic between the east coast of Barbados and the Northwest Tropical Atlantic Station (NTAS) mooring. Measurements of aerosol chemical, microphysical, optical, and cloud-nucleating properties were made during boreal winter onboard the *NOAA RV Ronald H. Brown* from 7 January to 13 February 2020. Observed aerosol properties indicate there were distinct periods when the aerosol was typical of clean marine conditions (particle number concentrations $<400 \text{ cm}^{-3}$, light absorption levels $<1 \text{ Mm}^{-1}$, and ^{222}Rn concentrations $<500 \text{ mBq m}^{-3}$) and when there were intrusions of dust mixed to varying degrees with biomass burning aerosol. In comparison to the long-term dust record at the Barbados Atmospheric Chemistry Observatory, the fraction of samples collected during ATOMIC with dust concentrations greater than $20 \mu\text{g m}^{-3}$ exceeded all years of the Barbados January to February record with the exception of 1983. The degree of mixing of the dust with biomass burning aerosol was modulated by the location of the North Atlantic subtropical high. A high located to the west of Africa led to a more northerly transport route and more dust-like (MDL) aerosol arriving at the ship. A location of the high further to the east over northern Africa led to a more southerly transport route and more biomass burning aerosol mixed with the dust. Properties for the marine, MDL, and mixed dust and biomass burning aerosol are presented.

1. Introduction

The ATOMIC study area extended in longitude from Barbados to the Northwest Tropical Atlantic Station (NTAS) mooring located at 51°W and in latitude from 13°N to 16°N . ATOMIC was conducted in collaboration with the European Elucidating the Role of Clouds Circulation Coupling in Climate Campaign (EUREC⁴A; Stevens et al., 2021). Four research vessels, four research aircraft, land-based measurements from two sites on Barbados, and multiple uncrewed seagoing and aerial vehicles participated in the combined ATOMIC and EUREC⁴A efforts. This paper focuses on the aerosol measurements made from the *NOAA RV Ronald H. Brown* (RHB) between 7 January and 13 February 2020. The NOAA ship and WP-3D (P-3) aircraft focused on the eastern portion of the combined EUREC⁴A and ATOMIC study areas to provide a view of the atmospheric and oceanic conditions upwind of the EUREC⁴A platforms (Figure 1). Most of the ATOMIC operations took place between 57°W and 51°W with the exception of an intercomparison with the Barbados Cloud Observatory (BCO) and the Barbados Atmospheric Chemistry Observatory (BACO) when the ship was located 20 NM to the east of Barbados.

ATOMIC was conducted in the boreal winter to study the role of marine boundary layer (MBL) convection and mixing in the formation of low level, shallow clouds at a time of year when other cloud types are mostly absent. Shallow clouds help mix boundary layer and free-tropospheric air, precondition the atmosphere for deeper convection, reflect incoming solar radiation, and cool the surface (Vial et al., 2016). Climate models have difficulty accurately parameterizing shallow clouds because of the subgrid scale nature of the processes involved in their formation (Bony et al., 2015). Improving the accuracy of models requires observations that will result in a better understanding of the boundary layer conditions that lead to the formation, extent, and lifetime of shallow clouds. Measurements of aerosol chemical, microphysical, optical, and cloud-nucleating properties are required to understand the impact of aerosol on clouds and vice versa and to improve the accuracy of model parameterizations.

Writing – original draft: P. K. Quinn
Writing – review & editing: L. M. Upchurch, J. E. Johnson, A. Brewer, S. Baidar, I. L. McCoy, P. Zuidema

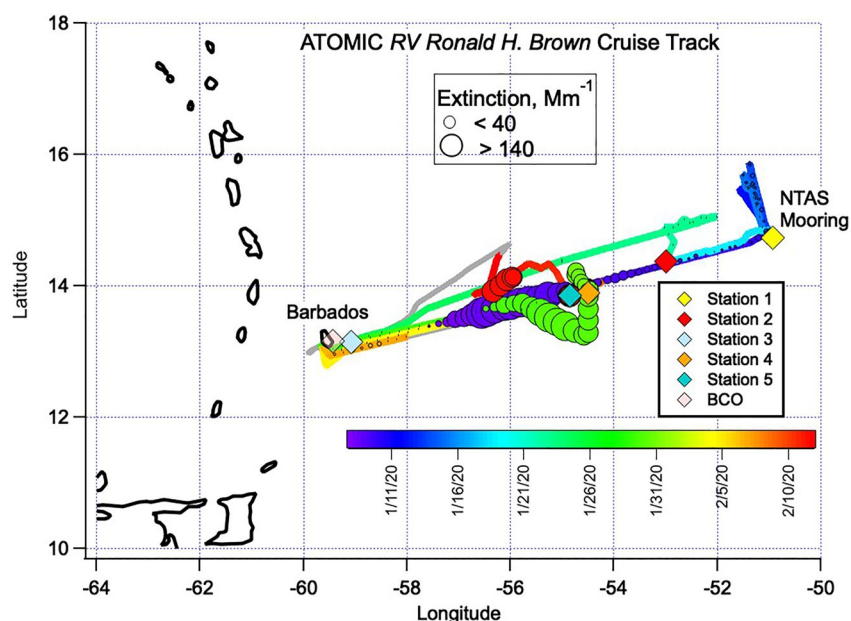


Figure 1. Cruise track of the NOAA RV Ronald H. Brown during ATOMIC colored by date (UTC) with markers sized by measured aerosol light extinction (light absorption plus scattering coefficients in Mm^{-1}). Stations where the ship spent time are indicated by diamond markers. BCO indicates the location of the Barbados Cloud Observatory and the Barbados Atmospheric Chemistry Observatory. The grayed portion of the track indicates where aerosol measurements stopped and the ship returned to Bridgetown at the end of the cruise.

Dust from North Africa is a major source of aerosol to the northwest tropical Atlantic (Prospero et al., 1970). Concentrations of dust have been measured on the easternmost coast of Barbados since 1965 (Prospero & Lamb, 2003). This long-term record shows maximum concentrations in boreal summer and minimum concentrations in winter (Prospero & Mayol-Bracero, 2013; Zuidema et al., 2019). Early satellite observations from the Moderate Resolution Imaging Spectroradiometer (MODIS) also showed seasonality in the transport of dust from Africa to the Caribbean (Kaufman et al., 2005). Concentrations of dust were found to be at a maximum in July centered around 20°N with transport to the Caribbean and Florida. Minimum concentrations were observed in boreal winter (December to January) with dust plumes centered near the equator. An analysis of 2 years of daily back trajectories with Barbados as the starting point found that during the dry season (December to May) ~50% of the 10-day trajectories originated north of 10°N and east of 55°W while in the wet season (June to November) the percentage increased to nearly 66% (Stevens et al., 2016). Most of those trajectories passed over the European and African continents during the wet season while only 8% did so during the dry season, agreeing with the seasonal pattern in dust concentrations observed at Barbados.

Satellite and modeling studies have provided details about seasonality in the altitude of dust transport across the Atlantic. A 4-year record of CALIPSO-derived aerosol distributions over the Atlantic indicated that during June-July-August (JJA), dust extends across the Atlantic to the Caribbean as far as 100°W (Adams et al., 2012) with initial maximum altitudes of 6 km. As the dust moves to the west, the core of the plume decreases in altitude to ~3.5 km. During winter (December-January-February or DJF), the dust plume shifts to the south relative to JJA with a maximum altitude of 3 km and the altitude of the center of the plume at 1.5 km. A 5-year simulation of dust transport from Africa across the Atlantic using a combination of Eulerian and Lagrangian diagnostics (Glaser et al., 2015) found that in boreal winter, dust is transported primarily within the trade wind layer toward South America while in summer, dust is transported to the Caribbean at higher altitudes.

Seasonality in the transport of dust across the Atlantic has been attributed to climate indices such as the El Niño Southern Oscillation (ENSO) index (Prospero & Lamb, 2003) and the North Atlantic Oscillation (NAO; Moulin et al., 1997), changes in synoptic systems over the eastern Atlantic and north Africa (Knippertz et al., 2011), and the seasonal shift in the Intertropical Convergence Zone (ITCZ) and associated large-scale winds (Doherty et al., 2012).

During the summer, a thermal low prevails over West Africa centered around 17°–23°N leading to vertical mixing of Saharan dust up to 5–6 km (Ben-Ami et al., 2009). As the dust layer moves west from the continent, it overrides the trade winds and forms the elevated Saharan Air Layer (SAL; Carlson & Prospero, 1972). As it transits over the Atlantic, it descends to 4–5 km eventually entering the MBL via entrainment and convective mixing (Weinzierl et al., 2017). The center of the summertime dust belt identified by the largest aerosol optical depths (AOD) occurs between 15°N and 20°N with transport to the Caribbean and Florida (Ben-Ami et al., 2009; Huang et al., 2010).

Synoptic systems over Africa move southward during winter relative to summer (Schepanski et al., 2009) leading to an intensification of Harmattan winds which are the dry northeasterlies that occur over the Sahara and Sahel in winter and spring (Knippertz et al., 2011). Intense Saharan dust storms result in the region of 5°–10°N. Due to lower insolation and less surface heating, dust is transported west within the trade wind layer at altitudes below 1.5–3 km. The center of the wintertime dust belt is around 5°–10°N extending to South America (Huang et al., 2010). Large emissions from biomass burning in the West Africa Sahelian region also occur in winter primarily due to agricultural activities (Cooke et al., 1996; Hao & Liu, 1994). Observations from numerous wintertime field campaigns (e.g., AMMA, DODO, DABEX) have documented layers of biomass burning aerosol aloft over western Africa with dust near the surface (Formenti et al., 2008; Johnson et al., 2008).

The CALIPSO analysis of Adams et al. (2012) also identified the presence of dust mixed with biomass burning smoke. In DJF, the mixed dust and biomass burning (MDBB) aerosol was found to encompass the ITCZ and extend longitudinally across the Atlantic due to mixing near the source regions, lofting to altitudes up to 4 km, and lower rainfall rates in winter which limit removal.

Several studies have focused on the role of the ITCZ and associated large-scale winds in the seasonal transport of both dust and biomass burning from Africa westward across the Atlantic (Adams et al., 2012; Doherty et al., 2012; Knippertz et al., 2011). Measurements made during the Barbados Oceanographic and Meteorological Experiment (BOMEX) conducted in May–July 1969 showed that the African dust plume was located directly to the north of the ITCZ (Prospero & Carlson, 1972). Later satellite observations (1982–2005) showed the dust belt lies to the north and heads to the Caribbean in the summer and moves to the south in the winter and heads toward South America (Evan et al., 2006) following the seasonal migration of the ITCZ. Doherty et al. (2012) pointed out that Barbados can receive dust in the winter since it lies on the northern edge of the plume as it is transported to the western tropical North Atlantic during that time of year.

Based on measured concentrations of trace elements (Al, Si, nonsea salt (nss) Ca, Fe, and Ti) and light scattering and absorption coefficients, dust was detected ~33% of the total time aerosol was sampled on the RHB between 8 January and 11 February. In addition, based on measured aerosol optical properties, biomass burning aerosol was mixed with the dust to varying degrees. Levels of observed dust are presented here in context with the long-term record from Barbados. During periods with little evidence of dust, the aerosol was composed of sea salt, organics, and nss sulfate. We focus here on characterizing the aerosol chemical, microphysical, optical, and cloud-nucleating properties observed during marine (M), more dust-like (MDL), and MDBB cases. Synoptic conditions and back trajectories are described for each case.

2. Methods

2.1. Aerosol Sampling Inlet

Sample air was drawn through a 5 m mast 18 m.a.s.l. and forward of the ship's stack. The mast inlet was automatically rotated into the wind to maintain nominally isokinetic flow. Air entered the inlet through a 5-cm diameter hole, passed through a 7° expansion cone, and then into the 20-cm inner diameter sampling mast. The flow through the mast was 1 m³ min^{−1}. The transmission efficiency of the inlet for particles with aerodynamic diameters <6.5 μm is greater than 95% (Bates et al., 2002).

The bottom 1.5 m of the mast was heated so that the sample air was at a relative humidity (RH) of 60 ± 5%. The temperature of the sample air was monitored at the base of the mast. RH was calculated based on measured temperature and dewpoint. Temperature was computer-controlled to maintain the RH near 60%. Stainless steel tubes extending into the heated portion of the mast were connected to aerosol instrumentation with conductive silicone tubing. Stainless steel tubing was used for aerosol collected for organic carbon (OC) analysis. Data

reported here were collected only when the particle number concentration, relative wind speed, and relative wind direction all indicated that there was no possibility of contamination from the ship's stack.

2.2. Aerosol Chemical Composition

Multijet cascade impactors (Berner et al., 1979) were used for the size segregated collection of aerosol. Air flow through the impactors was computer-controlled so that aerosol was only collected when the relative wind speed and direction and the particle number concentration indicated there was no contamination from the ship's stack. All sample handling was done in a glove box purged with air that passed through a scrubber containing potassium carbonate, citric acid, and activated charcoal to remove SO_2 , NH_3 , and volatile organics, respectively. Blank levels were determined by placing a substrate in the impactor with no air pulled through it. Concentrations of all aerosol chemical components are reported as $\mu\text{g m}^{-3}$ at 25 °C and 1,013 mb.

2.2.1. Inorganic Ions

A two stage impactor with 50% aerodynamic cut-off diameter, $D_{50,\text{aero}}$, of 1.1 and 10 μm at 60% RH was used for the collection of aerosol for analysis of inorganic ions (Na^+ , NH_4^+ , K^+ , Mg^{2+} , Ca^{2+} , Cl^- , NO_3^- , SO_4^{2-} , and methanesulfonate or MSA). A 12 μm grease cup was coated with silicone grease and a film coated with silicone spray was placed on the 10- μm jet place to minimize bounce of large particles onto downstream stages. Particles with diameters between 1.1 and 10 μm (supermicron) were collected on a Tedlar film. Particles with diameters <1.1 μm (submicron) were collected on Millipore Fluoropore filters (1.0- μm pore size). Films and filters were wetted with 1 mL of spectral grade methanol. Five milliliters of deionized water was then added to the solution and the substrates were extracted by sonicating for 30 min. Ion concentrations were determined by ion chromatography (Quinn et al., 1998).

nss SO_4^{2-} concentrations were calculated by subtracting sea salt SO_4^{2-} (based on measured Na^+ concentrations and the mass ratio of SO_4^{2-} to Na^+ in seawater of 0.252) from total measured sulfate. nss K^+ was calculated in a similar manner using the mass ratio of K^+ to Na^+ in seawater of 0.037.

Sea salt concentrations were calculated as

$$\text{Sea salt } (\mu\text{g m}^{-3}) = \text{Na}^+(\mu\text{g m}^{-3}) \times 1.47 + \text{Cl}^-(\mu\text{g m}^{-3}) \quad (1)$$

where 1.47 is the seawater ratio of $(\text{Na}^+ + \text{K}^+ + \text{Mg}^{2+} + \text{Ca}^{2+} + \text{SO}_4^{2-} + \text{HCO}_3^-)/\text{Na}^+$ (Holland, 1978). This approach prevents the inclusion of nss K^+ , Mg^{2+} , Ca^{2+} , SO_4^{2-} , and HCO_3^- in the sea salt mass and allows for the loss of Cl^- mass through Cl^- depletion processes (Quinn & Bates, 2005).

Sources of uncertainty in the ionic mass include the air volume sampled ($\pm 5\%$), the extract liquid volume ($\pm 3.3\%$), 2 times the standard deviation of the blank values measured over the course of the experiment, and the precision/calibration of the method ($\pm 5\%$). The average overall uncertainty was $\pm 8.5\%$.

2.2.2. Organic and Elemental Carbon

An impactor with $D_{50,\text{aero}}$ of 1.1 and 10 μm was used for the collection of submicron aerosol. A second impactor with $D_{50,\text{aero}}$ of 10 μm was used for collection of sub-10 μm aerosol. Precombusted (500 °C) quartz fiber filters were placed downstream of either the 1.1 μm (submicron) or 10- μm jet plates (sub-10 μm). Supermicron concentrations were derived from the difference between the two impactors. Carbon diffusion denuders were used upstream to avoid absorption of gas phase organics. A quartz filter downstream of the sample filter was used as a blank. Concentrations of OC and elemental carbon (EC) were determined with a Sunset Laboratory, Inc. thermal/optical analyzer (Birch & Cary, 1996). Three temperature steps were used to evolve OC under O_2 -free conditions (230, 600, and 870 °C). After cooling the sample down to 550 °C, a He/O_2 mixture was introduced and the sample was heated in four temperature steps to 910 °C to drive off EC. The transmission of light through the filter was measured to correct the observed EC for any OC that charred during the initial stages of heating.

Reported values of the ratio of organic matter molecular weight to OC weight (OM/OC) for marine and nonurban areas range from 1.6 up to 3.2. Some of the variability is likely due to methods used to determine the ratio including estimating organic matter molecular weight for different environments (Turpin & Lim, 2001), using a combination of nonrefractory (NR) organic mass concentrations from an Aerodyne Mass Spectrometer and OC mass concentrations from thermal volatility analysis (Bates et al., 2005, 2008), and organic functional group analysis

using FTIR spectroscopy (Lewis et al., 2021). An OM/OC ratio of 2.0 is used here to calculate total particulate organic matter (POM) from the measured OC concentrations. This value is based on previous NR AMS OM and thermal volatility-derived OC, the method used here for the measurement of OC.

Overall uncertainty in reported OC and EC concentrations is estimated at 13% and 9%, respectively.

2.2.3. Trace Elements

Two impactors containing 2.0- μm pore size PALL Teflo Membrane Disc Filters were used for the collection of aerosol for trace element quantification. One impactor had a $D_{50,\text{aero}}$ of 1.1 μm for the collection of sub-1.1 μm (submicron) aerosol. The other impactor had a $D_{50,\text{aero}}$ of 10 μm for the collection of sub-10 μm aerosol. Supermicron concentrations were determined by subtracting the sub-1.1 μm values from the sub-10 μm values. Energy dispersive X-ray fluorescence (ED-XRF) was used for the analysis of trace elements (Buck et al., 2021). Substrates were analyzed directly, i.e., without extraction. Aerosol covered 11.3 cm^2 of the 47-mm filter. No corrections were made for particle size or loading. Dust concentrations were calculated from Al, Si, Ca, Fe, and Ti, assuming that each element was present in the aerosol in its most common oxide form (Al_2O_3 , SiO_2 , CaO , K_2O , FeO , Fe_2O_3 , TiO_2 ; Seinfeld, 1986). The measured elemental mass concentration was multiplied by the appropriate molar correction factor as shown below (Malm et al., 1994; Perry et al., 1997)

$$[\text{Dust}] = 2.2[\text{Al}] + 2.49[\text{Si}] + 1.63[\text{Ca}] + 2.42[\text{Fe}] + 1.94[\text{Ti}]. \quad (2)$$

This equation includes a 16% correction factor to account for the presence of oxides of other elements such as K, Na, Mn, Mg, and V that are not included in the linear combination. In addition, the equation omits K from biomass burning by using Fe as a surrogate for soil K and an average K/Fe ratio of 0.6 in soil (Braaten & Cahill, 1986). Noncrustal K was calculated using the K/Al ratio (0.31) of Asian loess (Jahn et al., 2001) which is similar to the ratio in Saharan dust (0.24) and average crustal rock (0.32; Formenti et al., 2003). Sea salt Ca was accounted for based on the ratio of Ca to Na in seawater.

Sources of uncertainty in the dust concentrations include the volume of air sampled (5%), the area of the filter (5%), the molar correction factor (6%), 2 times the standard deviation of the blank values measured over the course of the experiment for each element, and the precision of the X-ray analysis. The average overall uncertainty was $\pm 11\%$.

2.3. AOD and Vertical Profile

A handheld Microtops Sunphotometer (Solar Light Co.) was used for the measurement of AOD at wavelengths of 380, 440, 500, 675, and 870 nm. The estimated AOD uncertainty at each wavelength did not exceed ± 0.02 (Knobelspiesse et al., 2004). Data were submitted to the NASA AERONET Maritime Aerosol Network. Information about data processing can be found at https://aeronet.gsfc.nasa.gov/new_web/man_data.html.

Vertical profiles of aerosol backscatter intensity and atmospheric vertical velocity were measured with a microjoule class, pulsed Doppler lidar (microDop) at a wavelength of 1.5 μm (Schroeder et al., 2020). The lidar, which was coupled to a motion stabilization platform, was mounted on the deck next to the aerosol sampling mast. It was motion stabilized while staring vertically to within 0.25° of zenith. Ship motion projected onto the line-of-sight velocity measurement was estimated and removed using a six-axis inertial navigation unit. The motion stabilization platform allowed the lidar to measure the mean and turbulent motions of aerosol in clear air and cloud scatterers with a spatial and temporal resolution of 33.6 m and 2 Hz, respectively. The first valid gate was 75 m above the ocean surface. The lidar typically provided data through the top of the MBL and, in the presence of dust, to altitudes higher than 3 km.

2.4. Aerosol Number Size Distribution

Particle number size distributions from 0.02 to 10 μm were measured at $60 \pm 5\%$ RH with a combination of three particle sizers. One of the mast tubes was used to supply sample air to a short column differential mobility particle sizer (Aitken-DMPS), a medium column DMPS (Accumulation-DMPS), and an aerodynamic particle sizer (APS, TSI 3321). The Aitken-DMPS and Accumulation-DMPS were short and medium column University of Vienna (Winklmeyer et al., 1991) instruments, respectively. Both DMPSs were connected to a TSI 3760A particle

counter and operated with a positive center rod voltage to sample particles with a negative charge. The Aitken-DMPS collected data in 10 size bins from 0.02 to 0.2 μm D_{gn} (geometric mean number diameter). It was operated with a sample air flow rate of 1 L min^{-1} and a sheath air flow rate of 10 L min^{-1} . The Accumulation-DMPS collected data in 7 size bins from 0.2 to 0.8 μm D_{gn} . It was operated with a sample air flow rate of 0.5 L min^{-1} and a sheath air flow rate of 5 L min^{-1} . The aerosol was charged with a Po^{210} charge neutralizer upstream of each DMPS. Mobility distributions were collected every 5 min. The mobility distributions were inverted to a number distribution assuming a Fuchs-Boltzman charge distribution from the Po^{210} charge neutralizer and corrected for multiple charge effects (Stratmann & Wiedensohler, 1997). The data were corrected for diffusional losses and size dependent counting efficiencies (Wiedensohler et al., 2007).

The APS was located at the base of the sampling mast and connected with a vertical inlet to minimize the loss of larger particles. Sample was drawn isokinetically from the larger flow to the DMPSs. Number size distributions were collected every 5 min. Data were collected in 34 size bins with aerodynamic diameters ranging from 0.96 to 10.37 μm .

The DMPS and APS size distributions were merged by converting the APS data from aerodynamic to geometric diameters using calculated densities and associated water mass at 60% RH based on the measured chemical composition (Quinn et al., 2002). The merged size distributions were fit with multiple lognormal modes using the lognormal fit function in IGOR Pro (WaveMetrics; Quinn et al., 2017). Number and volume size distributions were fit separately for better detection of the Aitken and accumulation modes in the number distributions and the coarse mode in the volume distributions. In each case, the dominant mode was fit first then fitting of all modes was iterated. The ability of the multimodal fit to reproduce the measured size distribution was assessed with a chi-square test. Only cases where the chi-square value was less than the critical value at a significance level of 0.05 were included in the analysis. Volume modal parameters are not reported for the Aitken mode as the fit routine did not detect sufficient volume in this size range for an accurate fit.

2.5. Aerosol Volatility

One of the mast tubes was used to supply sample air to a thermodenuder—Scanning Mobility Particle Sizer (SMPS) system (Bates et al., 2012; Wehner et al., 2002). A 30 L min^{-1} flow passed through an impactor with a $D_{50,\text{aero}}$ of 1.1 μm and then was subsampled at 5 L min^{-1} . The impactor, as with all impactors used in this study, contained a 10- μm jet plate to minimize bounce of larger particles onto downstream stages. The subsampled flow was drawn into two 2.2-cm ID tubes, one at ambient temperature and one heated to 230 $^{\circ}\text{C}$. The heated section was 0.61-m long resulting in a residence time in the heated tube of 2.8 s. At the end of the heated tube, the flow passed through a perforated stainless steel tube (0.55 m) surrounded by a sheet of carbon-impregnated paper to remove reactive gas phase species. The heated and unheated airflows were then isokinetically subsampled at the centerline at 2.0 L min^{-1} and passed through a nafion dryer. A valve switched the two flows every 5 min so that either the heated or the unheated sample entered the SMPS while the other flow went to a bypass line. Using one SMPS for both the heated and unheated sample prevented uncertainties due to differences in SMPS instruments. Size distributions were measured between 0.02 and 0.5 μm D_{gn} . In addition to the SMPS, the flows were sampled with a CN counter (TSI 3010) and Cloud Condensation Nuclei (CCN) counter (Droplet Measurement Technologies, DMT) for a measure of heated and unheated total particle number and CCN concentrations, respectively. Tests with ammonium sulfate aerosol showed that <10% of the total particle number concentration was reformed between the denuder and the SMPS with all of the reformation occurring at particle diameters <0.03 μm . This portion of the unheated and heated number size distributions (<0.03 μm) was omitted from the analysis.

2.6. CCN Activity

A DMT CCN Counter (CCNC) was used to determine CCN concentrations at supersaturations ranging from 0.1% to 0.62% (Lance et al., 2006; Roberts & Nenes, 2005). Concentrations at 0.1% and 0.4% are reported here as those supersaturations had the most values. An impactor with a $D_{50,\text{aero}}$ of 1.1 μm was upstream of the CCNC to sample the CCN activity of submicron bulk aerosol. The sampled air was dried prior to reaching the CCNC. The instrument was calibrated before and during the experiment using both $(\text{NH}_4)_2\text{SO}_4$ and NaCl as outlined by Lance et al. (2006). Based on these calibrations, reported supersaturations were decreased 0.04% below instrumental values. As described in Section 2.5, sample flow for the CCNC was switched between an unheated and

a heated (230 °C) inlet. At each supersaturation, the CCNC spent 5 min sampling unheated and 5 min sampling heated aerosol.

The critical diameter for CCN activation, D_{crit} , was defined as the particle diameter at which

$$\frac{CCN_{measured}}{CN_{integrated}} = 1.0, \quad (3)$$

where $CN_{integrated}$, the integrated condensation nuclei concentration, was found by integrating from the largest diameter measured by the SMPS down to the diameter where Equation 3 was satisfied. Uncertainty in Equation 3 and, therefore in D_{crit} , is estimated at $\pm 20\%$ based on a root sum of squares of the errors in the number concentrations derived from the CCN counter ($\pm 10\%$) and the measured size distributions ($\pm 18\%$). The actual uncertainty in D_{crit} will deviate from this estimate depending on the slope of the size distribution around D_{crit} , i.e., whether D_{crit} is greater than or less than the modal D_{gn} .

2.7. Aerosol Optical Properties

Measurements of aerosol scattering coefficients were made with integrating nephelometers (Model 3563, TSI Inc.) at wavelengths of 450, 550, and 700 nm. One nephelometer with a multijet cascade impactor ($D_{50,aero} = 10 \mu\text{m}$) upstream was used to measure sub-10 μm aerosol at 60% RH. A second nephelometer with an impactor ($D_{50,aero} = 1.1 \mu\text{m}$) upstream was used to measure submicron aerosol at 60% RH. A separate humidity-controlled system measured light scattering at two different relative humidities, 20% and 90%, with two nephelometers operated in series downstream of a multijet cascade impactor ($D_{50,aero} = 1.1 \mu\text{m}$). The first nephelometer in line measured sample air dried with a PermaPure, multiple-tube nafion dryer (model PR-94). Downstream of this nephelometer a humidifier was used to add water vapor to the sample flow using 6 microporous Teflon tubes surrounded by a heated water-jacket. Humidity was measured using a chilled mirror dew point hygrometer downstream of the second nephelometer in line. Span gas and CO_2 calibrations were performed on all nephelometers at the start of the experiment. During the cruise, particle-free air and CO_2 were analyzed every 3–4 days. The resulting zero offset and span factors were applied to the data. In addition, data were corrected for angular nonidealities of the nephelometer, including truncation errors and non-Lambertian illumination using the method of Anderson and Ogren (1998). Values are reported at 0 °C and 1,013 mb. For a 30 min averaging time and a wavelength of 550, a quadrature sum of errors yielded relative uncertainties at the 95% confidence level of $\pm 14\%$.

A Radiance Research Particle Soot Absorption Photometer (PSAP) at the outlet of the sub-10 μm nephelometer operated at 60% RH was used to measure the aerosol light absorption coefficient at 467, 530, and 660 nm. A PermaPure nafion dryer was placed upstream of the PSAP so that the sample air was at $\sim 25\%$ RH. Measured values were corrected for a scattering artifact, the deposit spot size, flow rate, and the manufacturer's calibration (Bond et al., 1999). Values are reported at 0 °C and 1,013 mb. For a 30 min averaging time and an absorption coefficient of 10 Mm^{-1} , a quadrature sum of errors yielded relative uncertainties at the 95% confidence level of $\pm 22\%$.

Aerosol light extinction was calculated as the sum of the measured scattering and absorption coefficients.

2.8. Radon

Radon (^{222}Rn —half-life of 3.82 days) was measured using the method of Whittlestone and Zahorowski (1998). Sample air was first drawn through a HEPA filter to remove all particles. A photomultiplier then counted the radon daughters produced in a 750 L decay tank for a 30-min period. The counts are proportional to ambient radon (not ambient radon daughters). The detector was standardized using radon emitted from a dry radon source (RN-25, PylonElectronics Corp.). Background counts were measured under conditions of zero air flow.

The rate of emission of radon from the ocean is ~ 100 times less than over land. As a result, ^{222}Rn is a qualitative tracer of an air mass that has been recently influenced by continental emissions (Carlson & Prospero, 1972). Here, a level of $^{222}\text{Rn} < 500 \text{ mBq m}^{-3}$ was considered indicative of an air parcel that had not been in recent convective contact with a continental surface. For comparison, ^{222}Rn concentrations for periods when dust was present ranged from 1,000 to 2,000 mBq m^{-3} .

2.9. Back Trajectories

The Hybrid Single-Particle Lagrangian Integrated Trajectory (HYSPPLIT) model (Stein et al., 2015) was used to calculate 7-day back trajectories for three arrival heights at the ship (100, 500, 1,000 m) using the Global Forecasting System (GFS) 0.25° model. The vertical velocity field was based on the meteorological data.

ERA5 reanalysis wind and surface level pressure fields were used to identify the location of synoptic systems influencing the calculated trajectories (CCCS, 2017).

2.10. Radiosondes

A total of 97 radiosondes (Vaisala RS41-SGP) were launched from the ship's fantail during Leg 1 and 66 were launched during Leg 2. There were six launches per day at 02:45, 06:45, 10:45, 14:45, 18:45, and 22:45 UTC. Vertical profiles were measured from the surface to ~25 km. Measurements were also made during the radiosondes' descents. The data were put into 10 m altitude bins and merged with the EUREC⁴A sounding network. Raw (Level-0), quality-controlled 1 s (Level-1), and vertically gridded (Level-2) data in NetCDF format are available at AERIS (<https://doi.org/10.25326/62>). The methods of data collection and postprocessing can be found in Stephan et al. (2020).

The lifted condensation level (LCL) calculated from the radiosonde vertical profiles was assumed to represent cloud base height and, therefore, the height of the well-mixed boundary layer. LCL (in m) was calculated as

$$\text{LCL} = (T_{50} - T_{d,50}) \times 125 + 50, \quad (4)$$

where T_{50} is temperature and $T_{d,50}$ is dew point, both at 50 m height (Bolton, 1980; Epsy, 1836). The lowest altitude considered was 50 m to avoid contamination by the temperature and relative humidity near the ship's deck and to minimize the effect of vertical gradients in the surface layer. Since the calculation started at 50 m, 50 was added to the LCL.

3. Results

3.1. Overview of Aerosol Observations

Measurements onboard the *NOAA RV Ronald H. Brown* during ATOMIC were conducted over the course of two legs. Leg 1 occurred between 8 and 25 January and Leg 2 between 29 January and 11 February with a scheduled port stop in Bridgetown, Barbados between 26 and 28 January. An additional break in sampling occurred between 3 and 6 February when the ship traveled back to Bridgetown for a medical emergency. More details about all atmospheric and oceanic measurements onboard, deployment of uncrewed assets, and interplatform comparisons can be found in Quinn et al. (2021).

There were distinct periods during ATOMIC when the aerosol was typical of clean marine conditions and when there were dust intrusions (Figure 2). The marine periods were defined by low particle number concentrations ($<400 \text{ cm}^{-3}$), light absorption levels ($<1 \text{ Mm}^{-1}$), and ^{222}Rn concentrations ($<500 \text{ mBq m}^{-3}$). Dust was first observed as an increase in light extinction on 8 January around 06:00 UTC when the ship was 120 NM east of the Barbados coast (Figures 1 and 2a). The highest sub-10 μm extinction levels of the cruise, 190 Mm^{-1} , were measured on 8 January around 20:00 UTC. Submicron and supermicron dust concentrations reached values of 13 and $23 \mu\text{g m}^{-3}$, respectively, before decreasing by an order of magnitude on 10 January as the ship continued a northeast transit to the NTAS mooring (Figures 2b and 2c). High dust concentrations were observed again during Leg 2 from 29 January until the ship transited downwind to Bridgetown for the medical emergency on 3 February and then again at the end of Leg 2 from 9 February until aerosol sampling was suspended on 11 February. Sub-10 μm extinction levels ranged between 70 and 170 Mm^{-1} during these periods and submicron and supermicron dust concentrations rose to 12 and $20 \mu\text{g m}^{-3}$, respectively. Over all dust periods, AOD ranged from 0.17 to 0.66 and averaged 0.42 ± 0.14 while CCN concentrations ($0.1\% \text{ S}$) ranged from 280 to 650 cm^{-3} and averaged $420 \pm 88 \text{ cm}^{-3}$ (Figure 2a).

During all dust periods, EC and nss K^+ were detected in the submicron aerosol (Figure 2b) and NO_3^- in the supermicron aerosol (Figure 2c), indicating the presence of biomass burning smoke (Gaudichet et al., 1995; Quinn et al., 2002).

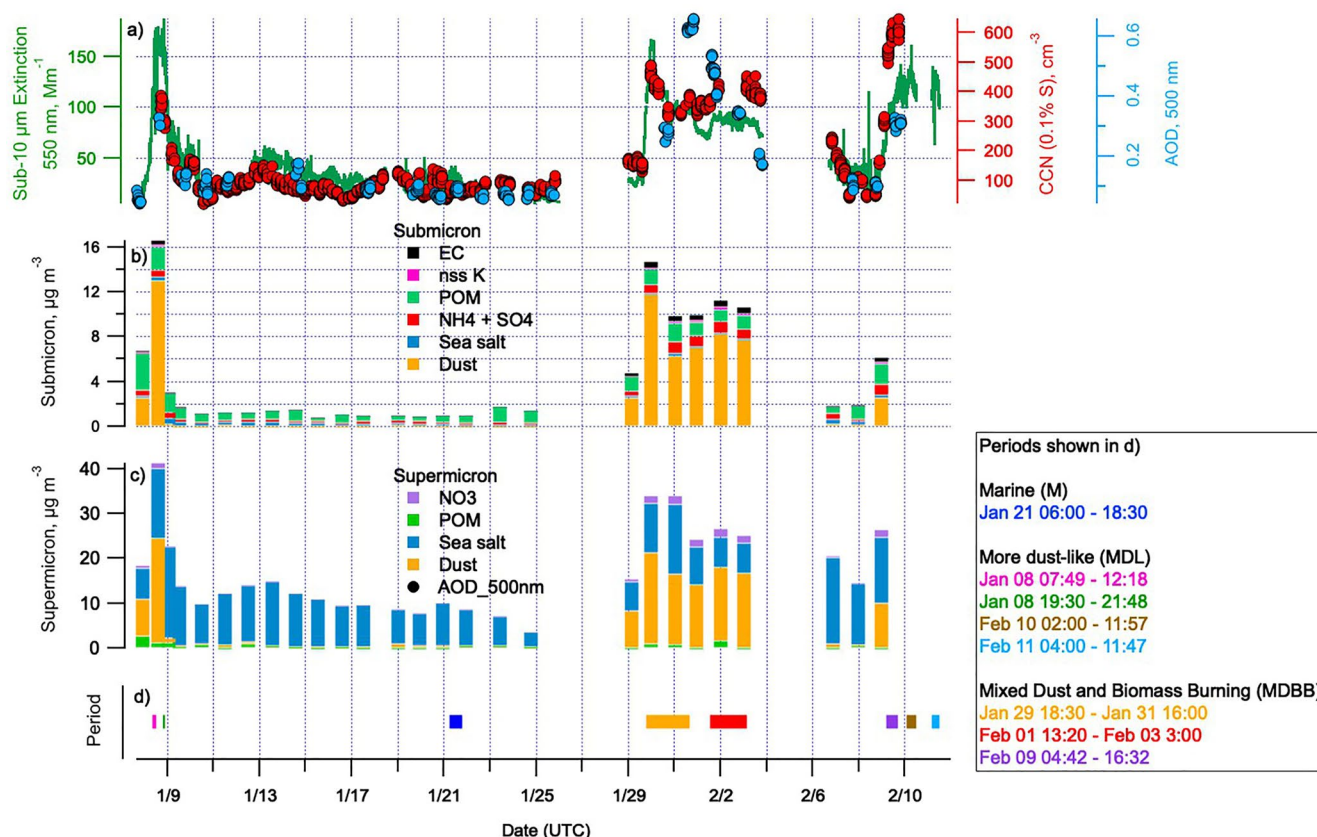


Figure 2. Time series of (a) sub-10 μm light extinction (scattering plus absorption), aerosol optical depth (AOD), and Cloud Condensation Nuclei (CCN) concentration at 0.1% supersaturation, (b) submicron and (c) supermicron mass concentration of chemical components, respectively, and (d) case study periods. Extinction values are 1-min averages, AOD is reported for every scan available, CCN concentrations are 10-s averages, and mass concentrations are reported for each impactor sampling period.

Marine aerosol was observed from 10 January through the end of Leg 1. During this time, the ship completed its transit to the NTAS mooring and then spent time near NTAS making atmospheric and oceanic observations until 17 January. The location of this first station and the mooring are shown in Figure 1. On 18 January, the ship transited downwind to Station 2 (Figure 1) and stayed in the area until 21 January. The ship then transited downwind to Station 3, 20 NM upwind of the Barbados Cloud Observatory (BCO) and Barbados Atmospheric Chemistry Observatory (BACO), for an interplatform comparison of aerosol, cloud, and meteorological parameters. Results of the comparison, which was conducted from 24 January 18:20 to 25 January 23:40 UTC, were reported by Quinn et al. (2021).

Sub-10 μm light extinction levels were $<60 \text{ Mm}^{-1}$ throughout the marine period (Figure 2a). Submicron aerosol was composed primarily of POM ($0.72 \pm 0.29 \mu\text{g m}^{-3}$), $\text{NH}_4^+ + \text{nss SO}_4^-$ ($0.19 \pm 0.06 \mu\text{g m}^{-3}$), and sea salt ($0.20 \pm 0.09 \mu\text{g m}^{-3}$; Figure 2b). Dust and EC concentrations were <0.07 and $0.05 \mu\text{g m}^{-3}$, respectively. The supermicron aerosol was dominated by sea salt ($9.3 \pm 2.8 \mu\text{g m}^{-3}$) with small contributions of dust ($0.22 \pm 0.23 \mu\text{g m}^{-3}$) and NO_3^- ($0.14 \pm 0.04 \mu\text{g m}^{-3}$; Figure 2c). Supermicron POM concentrations averaged ($0.27 \pm 0.28 \mu\text{g m}^{-3}$) while EC and nss K^+ concentrations were negligible ($<0.01 \mu\text{g m}^{-3}$).

During the marine periods, AOD ranged from 0.04 to 0.18 and averaged 0.09 ± 0.03 . CCN concentrations ranged from 20 to 250 cm^{-3} and averaged $89 \pm 26 \text{ cm}^{-3}$.

Time periods have been selected during the cruise to characterize properties of M, MDL, and MDBB aerosols. These time periods are indicated for reference in Figure 2d and will be discussed throughout the paper.

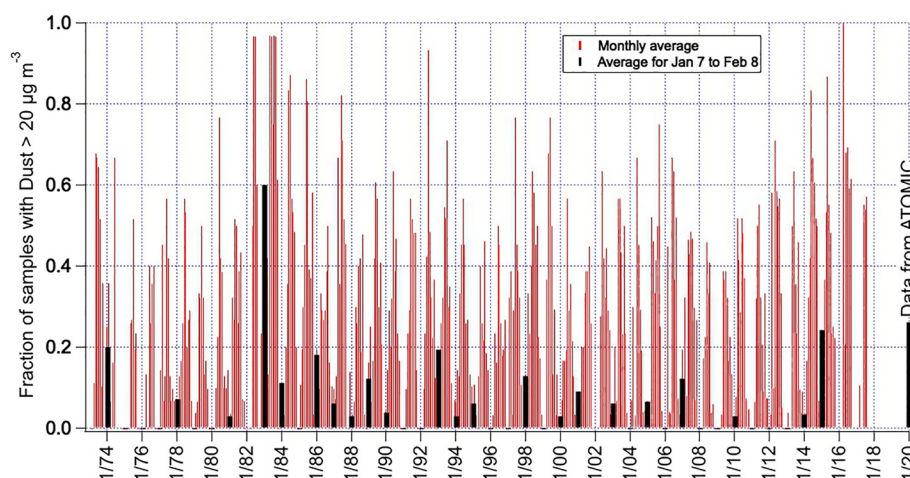


Figure 3. Monthly average of the fraction of samples collected at Ragged Point, Barbados ($13^{\circ}6'N$, $59^{\circ}37'W$) with measured dust concentration greater than $20 \mu\text{g m}^{-3}$. Also included is the average value from ATOMIC using the same threshold of $20 \mu\text{g m}^{-3}$.

3.2. ATOMIC Dust Concentrations Compared to the Barbados Long-Term Record

Dust concentrations have been measured at the Barbados Atmospheric Chemistry Observatory (BACO) at Ragged Point ($13^{\circ}6'N$, $59^{\circ}37'W$) on the east coast of Barbados since 1965. Here, we consider samples collected between 1973, when sampling with a high-volume sampler began, and 2017. Monthly mean concentrations of dust at Barbados during January and February, the months of the shipboard ATOMIC measurements, are 5.0 ± 5.8 and $6.0 \pm 5.5 \mu\text{g m}^{-3}$, respectively (Zuidema et al., 2019). For comparison, monthly mean concentrations during June, July, and August are 30 ± 11 , 25 ± 8.5 , and $20 \pm 6.3 \mu\text{g m}^{-3}$, respectively. The average sub- $10 \mu\text{m}$ dust concentration measured during ATOMIC was $7.7 \pm 12 \mu\text{g m}^{-3}$, slightly higher than the Barbados January and February average values. The upper size cut of the samples collected during ATOMIC was $10 \mu\text{m}$ while the high-volume sampler at Barbados has no upper cut-off limit. Without the upper size cut employed during ATOMIC, the difference between ATOMIC and BACO dust concentrations would likely be higher than reported here (Kramer et al., 2020).

To further evaluate how typical measured dust concentrations were during ATOMIC relative to the Barbados dust record, the number of episodes when dust concentrations exceeded $20 \mu\text{g m}^{-3}$ was compared. Figure 3 shows monthly averages of the fraction of samples collected with dust greater than $20 \mu\text{g m}^{-3}$ for all months of the long-term Barbados record and for ATOMIC. The same calculation was done using each year of the Barbados record from 7 January to 8 February to highlight the ATOMIC period. The lack of values for a given year indicates that no episodes occurred with measured dust concentrations greater than $20 \mu\text{g m}^{-3}$. ATOMIC's value exceeded all years of the Barbados record with the exception of 1983. High winter concentrations during 1982 and 1983 have been attributed to large-scale circulation changes associated with El Niño (Prospero & Nees, 1986).

Based on this comparison, the frequency of episodic dust events, as indicated by concentrations greater than $20 \mu\text{g m}^{-3}$, was higher during ATOMIC than normal for January and February.

3.3. Case Study Periods

3.3.1. Sub- $10 \mu\text{m}$ Intensive Aerosol Optical Properties

The case study periods shown in Figure 2d were chosen based on relatively uniform sub- $10 \mu\text{m}$ intensive aerosol optical properties measured throughout each period. The scattering Ångström exponent (SAE) was derived from measured light scattering coefficients (σ_{sp}) for the 450 and 700 nm nephelometer wavelength pair (λ_1 and λ_2 , respectively) as follows:

$$\text{SAE} = -\frac{\log(\sigma_{sp}(\lambda_1)/\sigma_{sp}(\lambda_2))}{\log(\lambda_1/\lambda_2)}. \quad (5)$$

Table 1

Average and Standard Deviation for the Case Study Periods of Submicron and Sub-10 μm Scattering Ångström Exponent (SAE; 450, 700 nm) and Single Scattering Albedo (SSA; 550 nm), the Submicron Humidity Dependence of Light Scattering ($f(\text{RH})$; 550 nm) and Fine Fraction of Scattering ($FF_{\sigma_{\text{sp}}}$; 550 nm)

Period (UTC)	Submicron			
	SAE (450, 700 nm)	SSA (550 nm)	$f(\text{RH}; 550 \text{ nm})$	$FF_{\sigma_{\text{sp}}} (550 \text{ nm})$
1/8/20 07:49–12:18 (MDL)	1.1 ± 0.12	0.72 ± 0.02	NA	0.14 ± 0.02
1/8/20 19:30–21:48 (MDL)	0.96 ± 0.08	0.75 ± 0.02	NA	0.13 ± 0.01
1/21/20 06:00–18:30 (M)	1.6 ± 0.83	0.97 ± 0.02	2.5 ± 0.30	0.05 ± 0.01
1/29/20 18:30–1/31/20 16:00 (MDBB)	1.5 ± 0.15	0.64 ± 0.02	1.2 ± 0.12	0.12 ± 0.01
2/1/20 13:20–2/3/20 03:00 (MDBB)	1.4 ± 0.11	0.62 ± 0.02	1.1 ± 0.05	0.17 ± 0.01
2/9/20 04:42–16:32 (MDBB)	1.8 ± 0.09	0.63 ± 0.01	1.2 ± 0.04	0.21 ± 0.01
2/10/20 02:00–11:57 (MDL)	1.6 ± 0.16	0.72 ± 0.01	1.3 ± 0.06	0.11 ± 0.01
2/11/20 04:00–11:47 (MDL)	1.6 ± 0.15	0.70 ± 0.01	1.4 ± 0.08	0.11 ± 0.01
	Sub-10 μm			
	SAE (450, 700 nm)	SSA(550 nm)		
1/8/20 07:49–12:18 (MDL)	-0.006 ± 0.03	0.91 ± 0.01		NA
1/8/20 19:30–21:48 (MDL)	-0.05 ± 0.02	0.92 ± 0.01		NA
1/21/20 06:00–18:30 (M)	-0.10 ± 0.05	0.99 ± 0.00		NA
1/29/20 18:30–1/31/20 16:00 (MDBB)	0.03 ± 0.03	0.90 ± 0.01		NA
2/1/20 13:20–2/3/20 03:00 (MDBB)	0.14 ± 0.03	0.86 ± 0.01		NA
2/9/20 04:42–16:32 (MDBB)	0.29 ± 0.05	0.86 ± 0.01		NA
2/10/20 02:00–11:57 (MDL)	-0.07 ± 0.05	0.93 ± 0.01		NA
2/11/20 04:00–11:47 (MDL)	-0.08 ± 0.04	0.93 ± 0.01		NA
2/11/20 04:00–11:47 (MDL)	NA	NA		NA

Note. NA, not available; MDL, more dust-like; MDBB, mixed dust and biomass burning; M, marine.

SAE is inversely proportional to particle size so larger values of SAE indicate a smaller particle size and vice versa.

Single scattering albedo (SSA) calculated as

$$\text{SSA} = \frac{\sigma_{\text{sp}}}{\sigma_{\text{sp}} + \sigma_{\text{ap}}} \quad (6)$$

is a measure of the relative magnitude of scattering (σ_{sp}) and absorption (σ_{ap}) by the aerosol. SSA is reported here at a wavelength of 550 nm.

Average and standard deviations of submicron and sub-10 μm SAE and SSA for each case study period are shown in Table 1. A regression of sub-10 μm SAE and SSA for the periods shows a continuum moving from high SSA and low SAE values to low SSA and high SAE (Figure 4). Marine aerosol resides in the upper left of the figure with high SSA (0.99 ± 0.003) and low SAE (-0.10 ± 0.05). This combination indicates a mostly scattering aerosol with larger particles dominating scattering as is typical of sea spray aerosol (Quinn et al., 2001, 2002). Sub-10 μm extinction for the M case was the lowest over all periods, ranging from 10 to 42 Mm^{-1} .

Periods on 8 January, 10 February, and 11 February are described here as MDL having average SAE values between -0.17 and 0.06 and average SSA values ranging from 0.88 to 0.95 . The low SAE values are similar to those measured for Saharan dust (-0.20 to 0.04) on aircraft flights over Sahelian West Africa during DABEX (Osborne et al., 2008) and 900 NM west of the African coast during the Aerosols99 cruise in the North Atlantic (-0.15 ± 0.06 ; Quinn et al., 2001). SSA values over all four periods are lower than values reported for dust during DABEX (0.99 ± 0.01 ; Osborne et al., 2008) and along the coast of Senegal during SHADE (0.97 ± 0.02 ; Haywood et al., 2003) and DODO-1 (0.99 ± 0.004 ; McConnell et al., 2008), indicating some degree of mixing

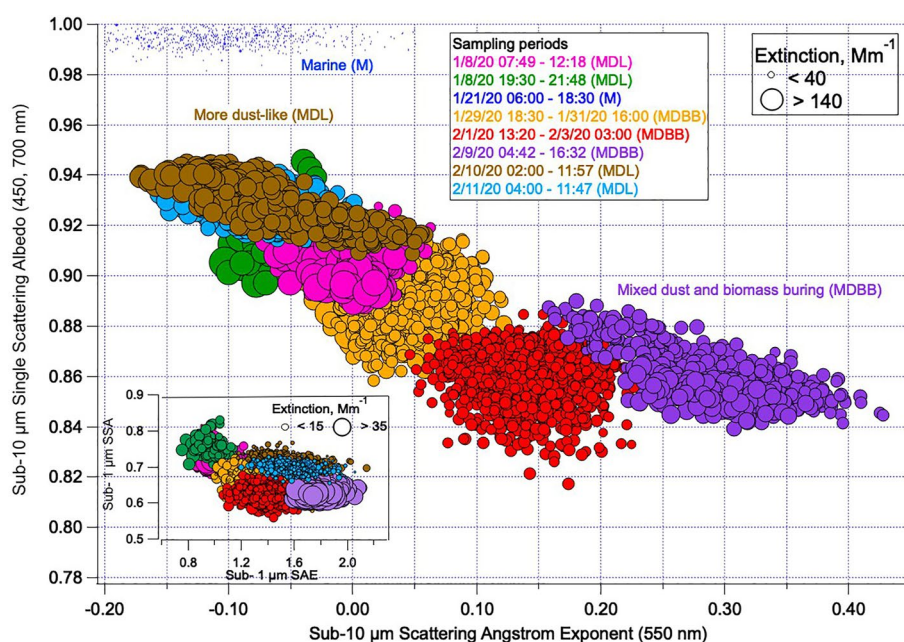


Figure 4. Regression of sub-10 μm scattering Ångström exponent (SAE; 450, 700 nm) and single scattering albedo (SSA; 550 nm) for each case study period. The size of the symbols corresponds to extinction level. M, marine; MDL, more dust-like; MDBB, mixed dust and biomass burning. The inset shows the regression of sub-1 μm SAE and SSA for each case study period.

with biomass burning aerosol. The presence of other nonbiomass burning combustion aerosols cannot be ruled out, however.

Periods beginning on 29 January, 1 February, and 9 February are described here as MDBB having higher SAEs and lower SSAs than the MDL periods, indicating the presence of a more absorbing, smaller diameter aerosol. Sub-10 μm SAE values ranged from -0.03 to 0.43 . This range is similar to the Aerosols99 values for MDBB aerosol (0.14 ± 0.19 ; Quinn et al., 2001) but smaller than values for biomass burning aerosol measured during Aerosols99 (0.71 ± 0.21) and DABEX (0.81 – 0.86 ; Osborne et al., 2008). SSAs ranged between 0.82 and 0.91 , similar to the average value for Aerosols99 MDBB aerosol (0.87 ± 0.05 ; Quinn et al., 2001).

3.3.2. Sub-1 μm Intensive Aerosol Optical Properties

Sub-1 μm SAE and SSA also were calculated for the case study periods (Table 1 and Figure 4). As expected, SAE values for the sub-1 μm size range are larger than the sub-10 μm size range spanning from 0.7 to 2.1 compared to -0.18 to 0.42 . In addition, the sub-1 μm SSA values are lower than the sub-10 μm values ranging from 0.52 to 0.85 compared to 0.82 to 0.95 . The sub-1 μm relationship between SAE and SSA for the case study periods is similar to that of the sub-10 μm aerosol with the exception of the MDL periods on 10 and 11 February. For these two cases, the SAE is higher and SSA is lower compared with the other two MDL cases on 8 January. The smaller diameter and more absorbing aerosol during the 10 and 11 February cases indicates a larger influence of biomass burning aerosol in the submicron size range relative to the sub-10 μm range compared to the other MDL cases. These two cases also have the lowest levels of submicron extinction for all dust case study periods, with the 9 February MDBB case having the highest

3.3.3. Relative Humidity Dependence of Scattering

The relative humidity dependence of scattering, or $f(\text{RH})$, of submicron aerosol was calculated as

$$f(\text{RH}) = \frac{\sigma_{\text{sp}}(\text{RH})}{\sigma_{\text{sp}}(\text{RH}_{\text{ref}})}, \quad (7)$$

where RH_{ref} and RH are the low and high relative humidities in the dual nephelometer $f(\text{RH})$ system of 20% and 90%, respectively. The average $f(\text{RH})$ for all marine periods was 2.5 ± 0.65 and for all periods when dust was

present (MDL and MDBB) was 1.2 ± 0.17 . Average $f(\text{RH})$ for the case study marine period was 2.5 ± 0.30 and ranged from 1.1 to 1.4 for the MDL and MDBB case study periods (Table 1). Burgos et al. (2019) summarized values of $f(\text{RH} = 85\%/\text{RH}_{\text{dry}})$ for particles with diameters <1 and $2.5 \mu\text{m}$ based on observations at long-term monitoring sites and during short-term field campaigns. Clean marine sites (Finokalia, Greece; Graciosa, Portugal; Trinidad Head, California, USA) were found to have the highest mean values ranging from 2.2 to 2.4. Values from the desert location of Niamey, Niger averaged 1.3 ± 0.14 .

3.3.4. Fine-Mode Fraction of Scattering

The light scattering coefficient of submicron and sub- $10 \mu\text{m}$ aerosol was measured separately since fine and coarse mode aerosol are chemically distinct and have different optical properties. The fine-mode fraction of scattering, $\text{FF}_{\sigma,\text{sp}}$ was calculated as

$$\text{FF}_{\sigma,\text{sp}} = \frac{\sigma_{\text{sp}, D < 1 \mu\text{m}}}{\sigma_{\text{sp}, D < 10 \mu\text{m}}}. \quad (8)$$

Ground-based and shipboard measurements of $\text{FF}_{\sigma,\text{sp}}$ have been used to evaluate and improve the fine-mode fraction of AOD retrieved from satellite observations (Kahn et al., 2004).

The average value of the $\text{FF}_{\sigma,\text{sp}}$ was lowest for the M case (0.05 ± 0.01) indicating sea spray aerosol with minimal accumulation mode continental influence (Quinn & Bates, 2005; Table 1). The average $\text{FF}_{\sigma,\text{sp}}$ was highest (0.21 ± 0.01) for the 9 February MDBB case corresponding to the highest observed levels of submicron extinction for all dust case study periods (Figure 4). The limited variability in $\text{FF}_{\sigma,\text{sp}}$ over all case study periods indicates the dominance of coarse mode aerosol in terms of mass concentration and light extinction throughout the experiment.

3.3.5. Synoptic Conditions

A synoptic map of surface level pressure (SLP) and wind speed at 1000 and 925 hPa, corresponding to ~ 170 and 840 m in altitude, respectively, was constructed for each case study period using ERA5 data sets. HYSPLIT back trajectories at three arrival heights at the ship (100, 500, and 1,000 m) were superimposed on the synoptic maps with the time of the map corresponding to the trajectory start time. One example typical of the M, MDL, and MDBB cases is shown in Figure 5.

For the M case, a composite synoptic map for 21 January 06:00 to 18:30 shows high-pressure systems were located over the southeast U.S. ($\sim 40^\circ\text{N}$ and 80°W) and the North Atlantic ($\sim 25^\circ\text{N}$ and 50°W ; Figure 5a). Back trajectories for all arrival heights followed the 1,000 and 925 hPa winds around the high over the U.S. bringing air from over the Canadian Arctic to the ship. The trajectories indicate subsidence from altitudes greater than 2,500 m to the surface. Air masses transported from the Arctic to the North Atlantic typically result in low particle number concentrations due to the lack of anthropogenic sources en route (Pennypacker & Wood, 2017; Quinn et al., 2019).

In all of the MDL cases, the subtropical high was centered near 35°N and between 40°W and 20°W , as shown in the composite synoptic map for 8 January 19:30 to 21:48 (Figure 5b). Air mass back trajectories roughly followed the 1,000 and 925 hPa winds around the high, descending to $<1,000 \text{ m}$ over Mali and then Mauritania, within the Sahara-Sahel dust corridor north of 15°N (Moreno et al., 2006). As previously reported, the approach of the subtropical high to northwestern Africa leads to dust transport to the Caribbean (Knippertz et al., 2011).

During the MDBB cases, the subtropical high was located further to the east than during the MDL cases. The synoptic map for the period that started on 1 February at 13:20 shows a high centered over the Iberian Peninsula and northern Africa (Figure 5c). The easterly location of the high resulted in air mass back trajectories following the 1,000 and 925 hPa winds at latitudes primarily south of 15°N over Africa and to the ship. Trajectories for the 500 and 1,000 m arrival heights took a more southerly course than did those for the 100 m arrival height.

Agricultural burning is prevalent across the sub-Saharan region of Africa during the dry season (Johnson et al., 2008a). NASA's Fire Information for Resource Management System (FIRMS), based on the Visible Infrared Imaging Radiometer Suite (VIIRS), indicates extensive fires in the sub-Saharan region during ATOMIC. Figure 5d shows an example from the 1 to 3 February period. The 1,000 m arrival height back trajectory for this period passed over sub-Saharan at high altitude ($>3,000 \text{ m}$) and then subsided into the boundary layer. The 100 m

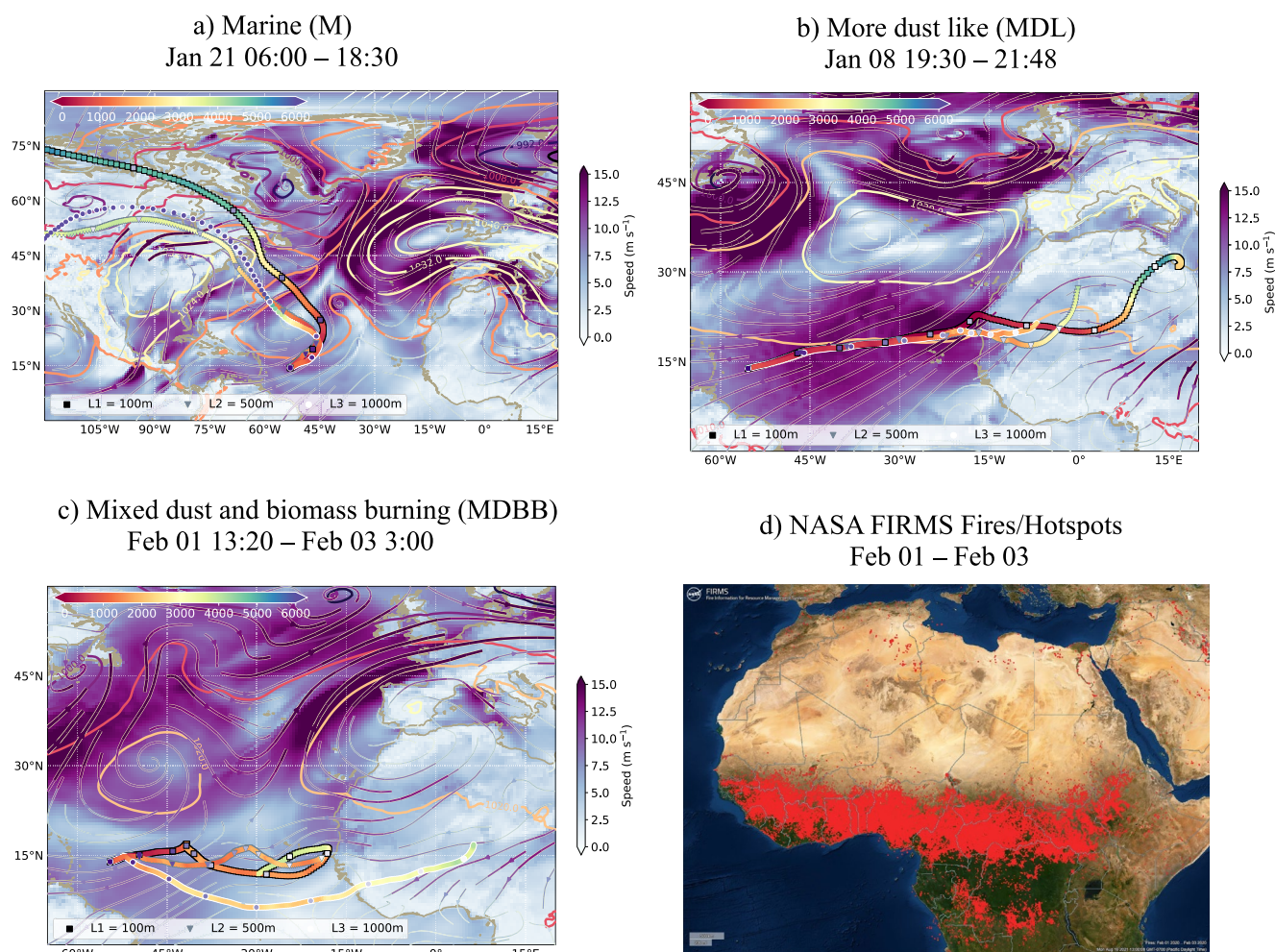


Figure 5. Synoptic conditions and calculated HYSPLIT back trajectories for (a) the marine (M) case of 21 January 06:00 to 18:30, (b) the more dust-like (MDL) case of 8 January 19:30–21:48, (c) the mixed dust and biomass burning (MDBB) case of 1 February 13:20 to 3 February 3:00, and (d) NASA FIRMS Fires/Hotspots for 1–3 February 2020 (<https://earthdata.nasa.gov/earth-observation-data/near-real-time/firms>). In (a)–(c), surface level pressure (SLP) is indicated by labeled contours. Wind speed at 1,000 hPa (~ 170 m) is indicated by colors and at 925 hPa (~ 840 m) by arrows using the same color convention. Back trajectories at three different arrival heights at the ship are overplotted as time versus height and colored by altitude. Each purple to white colored symbol along the trajectory indicates a 24-hr interval back in time from arrival at the ship. Note the different x and y axis scales in (a)–(c).

arrival height trajectory subsided from coastal sub-Saharan into the boundary layer before arriving at the ship. In both cases, and for the other MDBB cases, biomass burning aerosol was transported from higher altitudes over sub-Saharan and then mixed with dust as the air mass descended into the boundary layer.

3.3.6. Trajectory Analysis

A more quantitative analysis of the trajectories for each case study period was conducted to assess differences in transport. Eight-day trajectories, initiated every 4 hr during the M, MDL, and MDBB case study periods were binned into altitude bands of 0–1, 1–2, 2–3, and greater than 3 km. In addition, they were binned by latitudes north of 15°N and south of 15°N for longitudes spanning from 40°W and east to 50°E . Binned trajectories were then averaged over each period and the fraction of time spent in each altitude band and north or south of 15°N was calculated for each case study period. The results are shown in Figure 6 with the M case on the left, MDL cases in the middle, and the MDBB cases on the right.

The M case is unique due to the longitude restriction of 40°W and east to 50°E . Only 1,000 m arrival height trajectories from north of 15°N were within this longitude bin. For all other cases, both MDL and MDBB, a significant fraction of the 100 m arrival height trajectories spent time north of 15°N and at altitudes <1 km (Figure 6a). The fraction of time spent north of 15°N and at altitudes <1 km for the MDL cases ranged from 37%

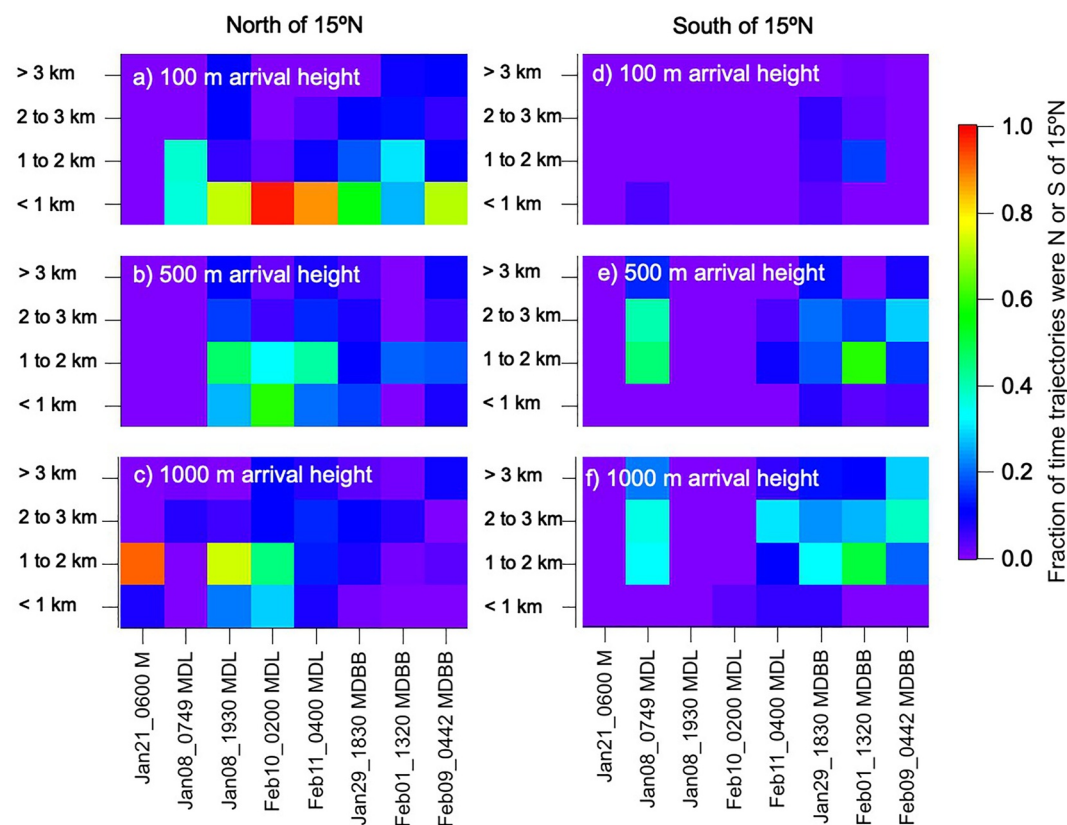


Figure 6. Fraction of time 8-day back trajectories spent north of 15°N for the (a) 100 m, (b) 500 m, and (c) 1,000 m arrival height at the ship's location and spent south of 15°N for the (d) 100 m, (e) 500 m, and (f) 1,000 m arrival height at the ship's location averaged over case study periods and binned into altitude bands of 0–1, 1–2, 2–3, and greater than 3 km. The marine (M) case is on the left of the plot, more dust-like cases (MDL) are in the middle, and the mixed dust and biomass burning (MDBB) cases are on the right.

to 87% and for the MDBB cases ranged from 26% to 72%. The location of the Sahara-Sahel dust corridor largely north of 15°N combined with persistent low altitude transport also from north of 15°N explains the presence of dust in all case periods considered.

The 500 and 1,000 m arrival height trajectories show a difference in transport for the MDL and MDBB cases. These trajectories for the MDL cases were predominantly from north of 15°N and at altitudes <2 km (Figures 6b and 6c). Exceptions include 8 January 07:49 to 12:18 and 11 February 04:00 to 11:47 UTC when 500 and 1,000 m arrival height trajectories spent some fraction of time (30–45%) south of 15°N at altitudes between 1 and 3 km (Figures 6e and 6f). During these two periods, the average 100 m arrival height trajectory spent 75% and 96%, respectively, of the 8-day transit in the 0–2 km altitude bands north of 15°N and transited from the Sahara-Sahel dust corridor to the ship, explaining the MDL optical properties.

The MDBB aerosol cases are associated with 500 and 1,000 m arrival height trajectories that had spent time south of 15°N and at altitudes higher than 1 km over the sub-Saharan region where agricultural burning is prevalent during the dry season (Johnson et al., 2008a; Figures 6e and 6f).

The location of the subtropical high, whether west of Africa or further to the east over northern Africa, modulates transport of aerosols along a more northerly or southerly route, respectively. In addition, the altitude of transport is impacted with higher altitudes being the main path for the more southerly route. The continuum of MDL and mixed dust with biomass burning sub-10 μm intensive optical properties in Figure 4 is a result of the variability in the location of the subtropical high and related transport patterns.

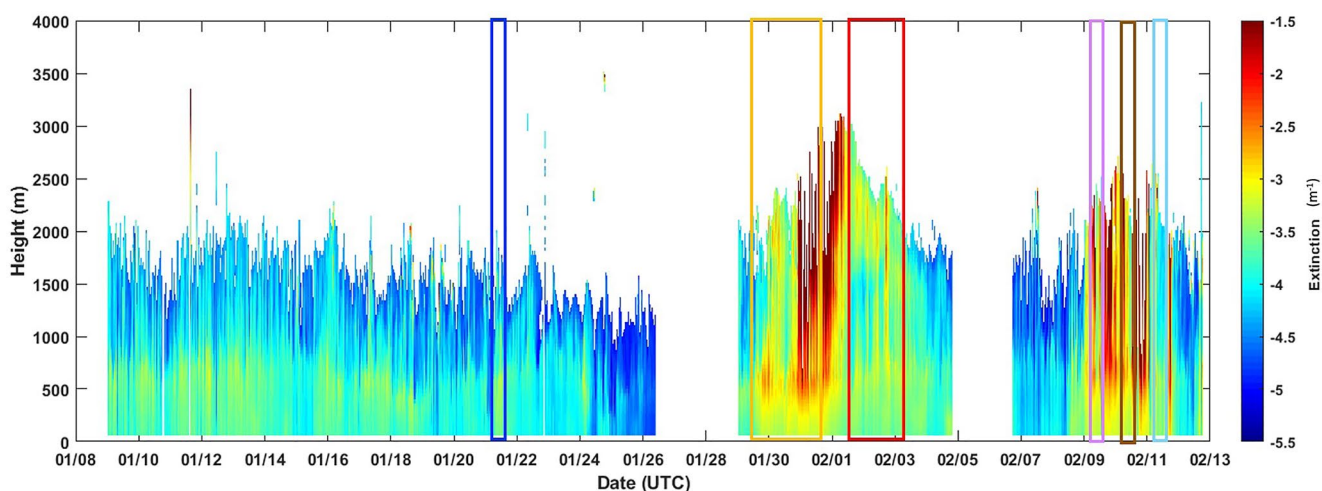


Figure 7. Extinction coefficient at 532 nm from the Doppler lidar. Case study periods are indicated as boxes with colors corresponding to the case study periods shown in Figure 4. No data are available for the 8 January periods.

3.3.7. Vertical Distribution of Dust During ATOMIC

The microDop lidar provided information on the aerosol vertical distribution directly overhead of the ship during ATOMIC (Figure 7). The aerosol backscattering coefficient was retrieved from the microDop range corrected intensity (RCI) profile following the method described in Chouza et al. (2015). The microDop RCI was calibrated using the Raman lidar measurements at the Barbados Cloud Observatory on 25 January 2020 when the RV Ronald H. Brown was stationed 20 NM upwind of BCO for instrument comparison. Lidar ratio values of 23 and 37, based on CALIPSO aerosol classification for marine and dust cases, respectively, were used to convert backscatter to extinction at 532 nm (Omar et al., 2009). The vertical velocity variance profiles (not shown) revealed a fairly uniform boundary layer height, defined as the bottom of the lowest cloud layer, around 750 m. Aerosol was detected within the boundary layer throughout the experiment with the largest loadings occurring during the MDL periods on 8, 10, and 11 January and the MDBB cases on 29–31 January and 9 February. A distinct higher altitude aerosol layer was detected by the lidar between ~1,500 and 2,500 m on 31 January to 3 February. Higher altitude aerosol was also observed between 9 and 11 February. These periods of higher altitude aerosol include the MDBB case study periods and are in good agreement with the trajectory analysis indicating transport to the ship at altitudes between 1,000 and 3,000 km.

Values of the sub-10 μm surface extinction coefficient and AOD were compared in a linear regression for all available AOD data (Figure 8). Time periods indicated in Figure 2d are highlighted by color. Time periods depicted by the gray symbols did not fall within the definition of M, MDL, or MDBB cases based on the correlation between sub-10 μm SAE and SSA shown in Figure 4. The marine period from 21 January and the MDBB case from 9 February fall on a regression line ($r^2 = 0.95$) with the majority of available data which includes the unclassified time periods. The correlation between surface extinction and AOD for these cases indicates that the aerosol was confined to a well-mixed MBL or that the MBL and upper layers of aerosol were well-mixed (Quinn et al., 2002). The lack of a correlation between AOD and surface extinction for the MDBB cases on 29–31 January and 1 February to third provides evidence of an upper layer of aerosol that is not well-mixed into the boundary layer, corroborating the lidar results (Figure 7).

The fraction of AOD due to aerosol in the MBL, AOD_{MBL} , was derived from measured AOD and in situ submicron scattering and absorption. $\text{FF}_{\sigma,\text{sp}}$ calculated from Equation 8 was used to adjust the submicron scattering measured at 20% RH to total sub-10 μm scattering.

The resulting sub-10 μm scattering at 20% RH was adjusted to ambient RH based on $f(\text{RH})$ calculated from Equation 7. The overall equation for calculating AOD_{MBL} was

$$\text{AOD}_{\text{MBL}} = \int_0^z (\sigma_{\text{sp,sub,20\%RH}} / \text{FF}_{\sigma,\text{sp}} \times ((1 - \text{RH}_{\text{ambient}}/100)^{-\gamma} + \sigma_{\text{ap,sub,dryRH}})) dz, \quad (9)$$

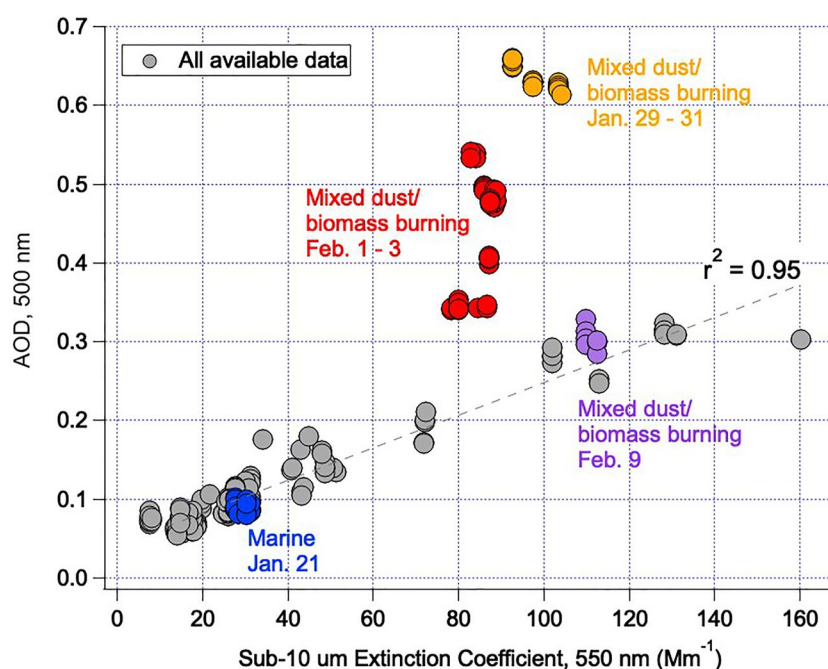


Figure 8. Regression of sub-10 μm extinction coefficient (550 nm) measured at the surface and aerosol optical depths (AOD; 500 nm). All available data are shown in gray and case study periods with available data are highlighted in color.

where $\sigma_{\text{sp,sub,20\%RH}}$ is the submicron light scattering coefficient measured at 20% RH, $\sigma_{\text{ap,sub,dryRH}}$ is the submicron light absorption coefficient measured at low RH. $\text{RH}_{\text{ambient}}$ is based on vertical profiles of RH from the radiosonde launched nearest in time to the AOD measurement, z is the height of the MBL based on the LCL from the radiosondes (Section 2.10), and γ is

$$\gamma = \ln \left(\frac{1}{f(\text{RH})} \right) / \ln \left(\frac{100 - \text{RH}_{\text{ref}}}{100 - \text{RH}} \right). \quad (10)$$

RH_{ref} and RH in Equation 10 are the low and high relative humidities in the dual nephelometer $f(\text{RH})$ system of 20% and 90%, respectively. Average $f(\text{RH})$ values for each case study period are reported in Table 1. The use of γ allowed the two-point RH measurements to be applied to the broader range of ambient RH values (Doherty et al., 2005; Quinn et al., 2005).

The highest fraction of AOD_{MBL} ($\text{AOD}_{\text{MBL}}/\text{measured AOD}$) was found for the marine period (0.50 ± 0.03). Based on the submicron and supermicron composition measurements, AOD_{MBL} was dominated by sea salt and associated organics (Figures 2b and 2c). Lowest fractions of AOD_{MBL} were calculated for the 29 January (0.04 ± 0.01) and 1 February (0.16 ± 0.01) MDBB cases which agrees with the lack of a correlation between surface extinction and AOD shown in Figure 8. The fraction of AOD_{MBL} for the 9 February MDBB case averaged 0.34 ± 0.01 . The correlation between surface extinction and AOD values during this period suggests that the MBL was well-mixed with the higher altitude aerosol layers.

3.3.8. Volume and Number Size Distributions

Averaged volume and number size distributions for the case study periods were lognormally fit as described in Section 2.4. The resulting fit parameters, including modal volume or number, diameter, and geometric standard deviation for the accumulation and coarse modes are listed in Table 2. Aitken modal parameters for the number size distributions are also provided in Table 2. Volume distribution accumulation modal diameters were similar for the MDL and MDBB cases ranging from 0.23 to 0.26 μm . The M case was distinct with a smaller accumulation mode diameter of 0.19 μm . Coarse modal diameters were similar for all cases ranging from 1.8 to 1.9 μm . More informative for understanding the sub-10 μm SAE is the fraction of the total volume in the accumulation mode, $V_{\text{acc}}/V_{\text{total}}$. The fraction was the lowest for the M case at 0.02 corresponding to low sub-10 μm SAE values. Ratios ranged between 0.03 and 0.05 for the MDL cases and, for the MDBB cases, from the high end of the MDL

Table 2

Lognormal Fit Parameters for the Volume and Number Size Distributions From the Merged DMPS and APS Data at 60% RH

Period (UTC)	dV/dlogD _p						
	Accumulation				Coarse		
	V _{acc} /V _{total}	V (μm ³ cm ⁻³)	D _{gn} (μm)	σ _{sg}	V (μm ³ cm ⁻³)	D _{gn} (μm)	σ _{sg}
1/8/20 07:49–12:18 (MDL)	0.04	2.4	0.26	1.6	55	1.9	1.85
1/8/20 19:30–21:48 (MDL)	0.03	2.1	0.26	1.6	72	1.9	1.84
1/21/20 06:00–18:30 (M)	0.02	2.5	0.19	1.5	15	2.0	1.89
1/29/20 18:30–1/31/20 16:00 (MDBB)	0.05	2.2	0.23	1.6	42	2.0	1.94
2/1/20 13:20–2/3/20 03:00 (MDBB)	0.08	2.7	0.24	1.6	32	1.8	1.94
2/9/20 04:42–16:32 (MDBB)	0.13	5	0.25	1.6	35	1.8	1.94
2/10/20 02:00–11:57 (MDL)	0.05	3	0.24	1.6	55	1.8	1.94
2/11/20 04:00–11:47 (MDL)	0.05	2.6	0.24	1.6	50	1.8	1.94

Period (UTC)	dN/dlogD _p								
	Aitken			Accumulation			Coarse		
	N (cm ⁻³)	D _{gn} (μm)	σ _{sg}	N (cm ⁻³)	D _{gn} (μm)	σ _{sg}	N (cm ⁻³)	D _{gn} (μm)	σ _{sg}
1/8/20 07:49–12:18 (MDL)	150	0.041	1.5	640	0.135	1.6	130	0.44	2.05
1/8/20 19:30–21:48 (MDL)	130	0.037	1.5	600	0.135	1.6	110	0.56	1.95
1/21/20 06:00–18:30 (M)	390	0.026	1.45	145	0.12	1.55	20	0.57	2
1/29/20 18:30–1/31/20 16:00 (MDBB)	190	0.046	1.45	905	0.125	1.6	100	0.49	1.95
2/1/20 13:20–2/3/20 03:00 (MDBB)	120	0.041	1.45	965	0.132	1.6	80	0.47	1.95
2/9/20 04:42–16:32 (MDBB)	85	0.032	1.4	1,505	0.132	1.65	100	0.46	1.95
2/10/20 02:00–11:57 (MDL)	165	0.034	1.4	1,165	0.117	1.65	110	0.46	2.05
2/11/20 04:00–11:47 (MDL)	145	0.035	1.41	1,005	0.127	1.65	100	0.46	1.95

Note. Volume distribution modal fit parameters include volume concentration (V), diameter (D_{gn}), and geometric standard deviation (σ_{sg}) for the accumulation and coarse modes. The fraction of the total volume in the accumulation mode (V_{acc}/V_{total}) also is shown. Number distribution fit parameters include number concentration (N), D_p , and σ_{sg} for the Aitken, accumulation, and coarse modes. MDL, more dust-like; MDBB, mixed dust and biomass burning; M, marine.

cases (0.05) to 0.13, following the general trend of sub-10 μm SAE shown in Figure 4. This result is similar to that of Shuster et al. (2006) who reported that SAE can be more sensitive to V_{acc}/V_{total} than modal diameter.

Number distribution modal parameters are discussed in Section 3.3.10 in the context of the CCN measurements.

3.3.9. Chemical Composition

A time series of absolute submicron and supermicron concentrations of chemical species for ATOMIC are shown in Figure 2 along with demarcations of the case study periods. Concentrations of all species except sea salt were lowest for the M period explaining the low extinction coefficient values shown in Figures 2 and 4. The largest surface extinction values correspond to the large dust concentrations of the MDL period starting on 8 January at 19:30 and the MDBB case starting on 29 January. To provide chemical confirmation for the designation of the MDL and MDBB cases, mass ratios of nss K⁺/Dust, NO₃⁻/Dust, and EC/Dust were calculated from the impactor sample that most overlapped in time with each case study period (Table 3).

Of the three ratios, only nss K⁺/Dust and NO₃⁻/Dust were calculated for the supermicron size range since supermicron EC was below the detection limit. Unfortunately, no impactor samples were available for the MDL periods on 10 and 11 February.

The MDBB cases had higher supermicron ratios of nss K⁺/Dust and NO₃⁻/Dust than the MDL cases indicating a larger influence from biomass burning. The difference is not as clear for the submicron size range although all three ratios are highest for the 9 February case which also had the largest sub-10 μm SAE, indicating smaller particles more typical of biomass burning than dust (Osborne et al., 2008; Shuster et al., 2006).

Table 3

Submicron and Supermicron Mass Ratios of $\text{Nss K}^+/\text{Dust}$ and $\text{NO}_3^-/\text{Dust}$ and Submicron Mass Ratios of EC/Dust for Case Study Periods With Available Impactor Composition Measurements

Period (UTC)	Mass ratio				
	Submicron			Supramicron	
	$\text{Nss K}^+/\text{Dust}$	$\text{NO}_3^-/\text{Dust}$	EC/Dust	$\text{Nss K}^+/\text{Dust}$	$\text{NO}_3^-/\text{Dust}$
1/8/20 07:49–12:18 (MDL)	0.04 ± 0.01	0.01 ± 0.002	0.08 ± 0.02	0.002 ± 0.001	0.08 ± 0.02
1/8/20 19:30–21:48 (MDL)	0.02 ± 0.01	0.005 ± 0.001	0.03 ± 0.01	0.002 ± 0.001	0.06 ± 0.01
1/29/20 18:30–1/31/20 16:00 (MDBB)	0.03 ± 0.01	0.01 ± 0.002	0.09 ± 0.02	0.004 ± 0.001	0.12 ± 0.02
2/1/20 13:20–2/3/20 03:00 (MDBB)	0.03 ± 0.01	0.01 ± 0.002	0.08 ± 0.02	0.004 ± 0.001	0.11 ± 0.02
2/9/20 04:42–16:32 (MDBB)	0.07 ± 0.02	0.02 ± 0.004	0.18 ± 0.04	0.003 ± 0.001	0.16 ± 0.03
2/10/20 02:00–11:57 (MDL)	NA	NA	NA	NA	NA
2/11/20 04:00–11:47 (MDL)	NA	NA	NA	NA	NA

Note. NA, not available; MDL, more dust-like; MDBB, mixed dust and biomass burning; M, marine. Combined uncertainties for the ratios are based on uncertainties provided for the chemical species in Section 2.

The lack of composition data for the 10 and 11 February MDL periods prevents a chemical explanation for the difference between submicron and sub-10 μm values of SAE and SSA shown in Figure 4.

3.3.10. CCN

CCN measurements were made during five of the eight case study periods (MDL: 8 January 19:30, M = 21 January, MDBB = 29 January, 1 February, 9 February). Figure 9a indicates the case study periods and Figure 9b shows CCN concentrations at two supersaturations (S). Lowest CCN concentrations at 0.1% S were measured during the M case ($96 \pm 6 \text{ cm}^{-3}$) with concentrations at 0.4% S being 30% higher ($140 \pm 7.6 \text{ cm}^{-3}$). CCN concentrations for the one MDL case with data available were $195 \pm 8 \text{ cm}^{-3}$ at 0.1% S. Concentrations at 0.4% S were not available. Highest CCN concentrations were measured during the three MDBB cases at 470 ± 54 , 320 ± 1 , and $440 \pm 36 \text{ cm}^{-3}$ for the periods beginning on 29 January, 1 February, and 9 February, respectively. Concentrations at 0.4% S were only 9.6%, 8.9%, and 12% higher for the three cases indicating a less soluble aerosol than for the M case. Higher CCN concentrations for cases with more biomass burning aerosol is consistent with results of CCN measurements made at Virginia Key, an island east of Miami, FL (Edwards et al., 2021).

The CCN population resides primarily in the accumulation mode size range (~ 50 – 300 nm at 60% RH). Directly determining the chemical composition of particles in this size range from the impactor samples is difficult due to low mass concentrations. Composition of the total particle concentration (CN) and CCN can be inferred, however, by measuring heated (230°C) and unheated number concentrations and calculating the volatile CN ($\text{CN}_{\text{Vol-NF}}$) and CCN ($\text{CCN}_{\text{Vol-NF}}$) number fraction, respectively. The CN volatile fraction was calculated as

$$\text{CN}_{\text{Vol-NF}} = \frac{(\text{Unheated CN} - \text{Heated CN})}{\text{Unheated CN}}, \quad (11)$$

where CN is the number concentration. The CCN volatile fraction was calculated similarly.

As discussed in Section 2.5, $\text{CN}_{\text{Vol-NF}}$ was calculated for dry particle diameters greater than 30 nm to avoid the possibility of interference from particle reformation between the thermal denuder and the SMPS. $\text{CN}_{\text{Vol-NF}}$ was highest for the marine period (0.77 ± 0.15) due to the large number concentration in the Aitken mode (390 cm^{-3}) of apparently volatile material (Figure 9c and Table 2). $\text{CN}_{\text{Vol-NF}}$ was lowest for the MDBB case on 9 February (0.21 ± 0.04) corresponding to evidence of refractory material at 230°C based on the low submicron SSA (0.63 ± 0.01 , Table 1) and a relatively high submicron EC to Dust ratio (0.18, Table 3). The two other MDBB cases had slightly higher $\text{CN}_{\text{Vol-NF}}$ (0.35 ± 0.07 and 0.33 ± 0.07 for the periods starting on 29 January and 1 February, respectively). The MDL had values ranging from 0.3 to 0.4.

The $\text{CCN}_{\text{Vol-NF}}$ followed a similar pattern as $\text{CN}_{\text{Vol-NF}}$ with the volatile fraction being highest for the M case at 0.91 for both 0.1% and 0.4% S (Figure 9c). For the MDL and MDBB cases, the $\text{CCN}_{\text{Vol-NF}}$ was lower at 0.4% than 0.1% S. The difference was greatest for the MDBB case on February 9th where $\text{CCN}_{\text{Vol-NF}}$ was 0.35 ± 0.07 at

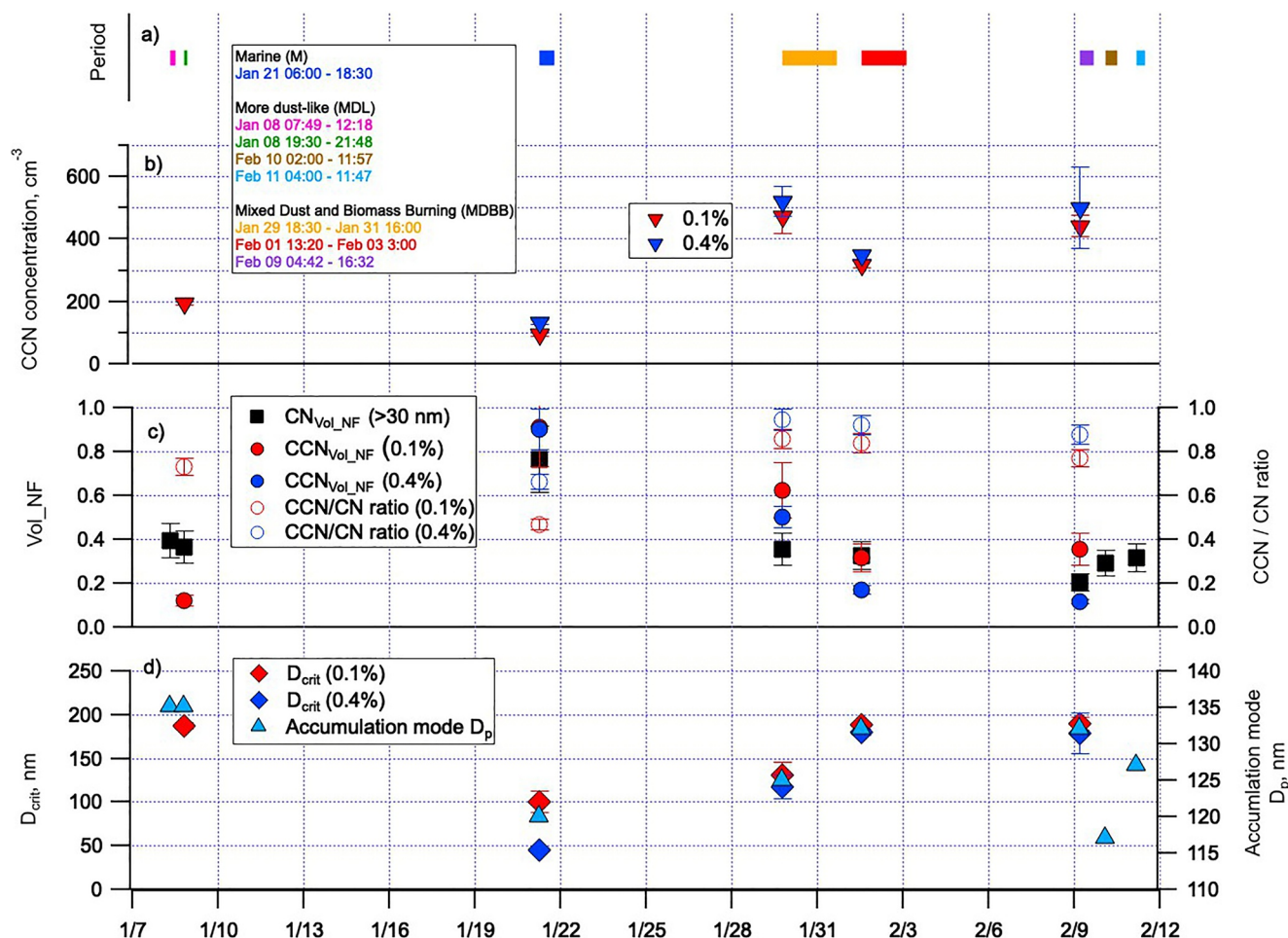


Figure 9. CN and CCN data for the case study periods with (a) times of periods, (b) CCN concentrations at 0.1% and 0.4% S, (c) CN volatile number fraction (CN_{Vol-NF}) for diameters greater than 30 nm, CCN volatile number fraction (CCN_{Vol-NF}), and CCN/CN activation ratio for 0.1% and 0.4% S, and (d) critical diameters at 0.1% and 0.4% S and accumulation mode diameters from the lognormal fit procedure. Vertical lines indicate $\pm 1\sigma$ standard deviation.

0.1% S and 0.12 ± 0.01 at 0.4% S. An increase in supersaturation from 0.1% to 0.4% led to smaller, nonvolatile particles being activated. The other MDBB cases also had detectable differences in CCN_{Vol-NF} at 0.1% and 0.4% S indicating appreciable refractory material at smaller particle sizes. Unfortunately, CCN measurements at 0.4% S were not available for any MDL cases.

Activation ratios (CCN/CN) were lowest for the M case (0.47 ± 0.02 at 0.1% S and 0.66 ± 0.03 at 0.4% S, Figure 9c). The M case also had the largest difference in the activation ratio at 0.1% and 0.4% S due to the large number concentration in the Aitken mode. Activation ratios for the MDL and MDBB cases were similar ranging from 0.73 to 0.86 at 0.1% S and 0.87 to 0.95 at 0.4% S. The larger values compared to the M case are due to larger accumulation mode diameters and relatively higher number concentrations in the accumulation mode compared to the Aitken mode (Table 2).

Using the method described in Section 2.6, critical diameters at 0.1% and 0.4% S were calculated from the measured size distribution and CCN concentration. Although activation ratios were lowest for the M case due to high Aitken mode number concentrations, D_{crit} values also were lowest (100 and 45 nm for 0.1% and 0.4% S, respectively) confirming a composition of soluble material (Figure 9c). D_{crit} values for the MDL and MDBB cases ranged from 130 to 190 nm. Values at 0.1% and 0.4% S were similar indicating a less soluble composition than the M case in agreement with lower SSAs and the measured dust and EC content.

4. Discussion

Shipboard measurements of aerosol properties made during ATOMIC provide evidence for the wintertime transport of Saharan dust to the Caribbean. As shown in Figure 3, dust is often detected at the Barbados Atmospheric Chemistry Observatory (BACO) in January and February but at much lower concentrations than during summer (Zuidema et al., 2019). The frequency of episodic dust events, defined as concentrations greater than $20 \mu\text{g m}^{-3}$, was higher during ATOMIC than previous January to February periods since measurements began at BACO with the exception of 1983. The high frequency of episodic dust events in 1983 has been attributed to El Niño and related North African drought conditions (Prospero & Nees, 1986).

An assessment of the numerous factors controlling dust emission and dust transport to the Caribbean is required to determine reasons for the number of episodic dust events during the winter of 2020. These reasons may include synoptic conditions tied to the NAO. The seasonally averaged NAO for winter 2020 (December 2019 to February 2020) was positive with values up to 1.0. (Seasonally averaged values since 1950 range from ~ -2 to 2, <https://www.climate.gov/news-features/understanding-climate/climate-variability-north-atlantic-oscillation>.) Previous studies have shown a positive correlation between the NAO and Saharan dust outbreaks over the North Atlantic during winter (Chiapello et al., 2005). Using monthly mean Aerosol Index (AI) values from the Total Ozone Mapping Spectrometer (TOMS) and NAO values, Nakamae and Shiotani (2013) found winter time positive NAO values correlated with high dust loadings over the North Atlantic. The positive correlation was attributed to wind speeds enhanced by the NAO over dust source regions and subsequent transport to the ocean.

The regression of sub- $10 \mu\text{m}$ Ångström Exponents versus SSA shown in Figure 4 reveals the occurrence of a continuum of high SSA-low SAE aerosol to lower SSA-higher SAE aerosol corresponding to MDL and MDBB aerosol, respectively. For the most part, the high SSA-low SAE aerosol also had lower submicron EC to dust and supermicron nss K^+ to dust mass ratios providing further evidence for an MDL aerosol. The lower SSA-higher SAE aerosol had higher submicron EC to dust, supermicron nss K^+ to dust, and supermicron NO_3^- to dust mass ratios as would be expected for MDBB aerosol. Aerosol with the highest SSA-lowest SAE stood out as typical of sea spray aerosol.

Synoptic conditions during the M case were dominated by a high-pressure system over the southeast U.S. that drew upper-level air from the Canadian Arctic to the south where it descended into the boundary layer in the northwest tropical Atlantic. At the same time, a high-pressure system was centered over the North Atlantic outside of the subtropics near 50°N . During the MDL cases, the subtropical high was centered near 35°N and between 40° and 20°W over the North Atlantic (Figure 5). Back trajectories with 100, 500, and 1,000 m arrival heights at the ship spent the majority of transit time north of 15°N in the region of the Sahara-Sahel dust corridor. Altitudes of transport were confined primarily to <2 km. During the MDBB cases, the subtropical high was located to the east over the Iberian Peninsula and north Africa. Trajectories spent a larger fraction of time south of 15°N and transport occurred at altitudes between 1 and 3 km. The more southerly transport route led to the mixture of biomass burning aerosol from the sub-Saharan region and dust that was eventually sampled on the ship. Vertical profiles of aerosol extinction (Figure 7) and the comparison of sub- $10 \mu\text{m}$ extinction measured at the surface with AOD (Figure 8) confirmed the presence of aerosol layers aloft during the MDBB cases.

The link between the location of the wintertime subtropical high and the transport of either MDL or MDBB aerosol to the eastern North Atlantic has been previously reported (Knippertz et al., 2011). Measurements conducted during January and February 2008 at Cape Verde during the second Saharan Mineral Dust Experiment (SAMUM-2) revealed a close relationship between the strength and position of the subtropical high over the North Atlantic and Africa and dust concentrations offshore. During the three major dust events that occurred (AOD values greater than 0.5), the subtropical high over the North Atlantic moved east over the Sahara strengthening winds and resulting in the transport of dust to Cape Verde. Knippertz et al. (2011) also reported that synoptic scale circulation was the main factor controlling the amount of biomass burning aerosol reaching Cape Verde. ATOMIC data show the influence of the same synoptic scale circulation on the occurrence of MDL and MDBB aerosol reaching the western tropical North Atlantic. Both at Cape Verde and in the ATOMIC study area, the lack of a subtropical high or the presence of a weak subtropical high over the North Atlantic resulted in clean marine aerosol being the dominant observed aerosol type.

The stable MBL height over the northwest tropical Atlantic allows for a direct comparison of the CCN concentration associated with each aerosol type. CCN concentrations were lowest for the M case at 0.1% S ($96 \pm 6 \text{ cm}^{-3}$)

but increased by 30% at 0.4% S indicating a soluble aerosol. Number concentrations were low due to the clean marine conditions. In addition, the majority of the particles that were present were in the Aitken mode with sizes smaller than the estimated critical diameter for activation (100 and 45 nm at 0.1% and 0.4% S, respectively). The CCN volatile fraction at 230 °C was 0.91 for both 0.1% and 0.4% indicating an Aitken mode composed of ammonium sulfate and organics.

CCN concentrations for the one MDL case with available data were $190 \pm 8 \text{ cm}^{-3}$ at 0.1% S. Concentrations at 0.4% S were not available. The accumulation mode dominated the number concentrations. The CCN volatile fraction was 0.1 at 0.1% S indicating that the majority of the CCN was composed of refractory material, presumably dust, at 230 °C. The average activation ratio was high (0.73 ± 0.1) due to the accumulation modal diameter being larger than the critical diameter for activation (190 nm).

Highest CCN concentrations, with average values ranging from 320 to 440 cm^{-3} , were measured during the three MDBB cases. Concentrations at 0.4% S were only about 10% higher than those measured at 0.1% S indicating a less soluble aerosol than for the M case. As for the MDL cases, the accumulation mode dominated the size distribution. For all MDBB cases, the CCN volatile fraction was higher at 0.1% than 0.4% S. An increase in supersaturation led to smaller, nonvolatile particles (at 230 °C) being activated. Activation ratios were high at 0.8 and above due to accumulation modal diameters being similar to estimated critical diameters.

5. Conclusions

ATOMIC was conducted in the northwest tropical Atlantic between Barbados and the NTAS mooring ($\sim 51^\circ\text{W}$) during boreal winter (7 January to 13 February 2020) to assess formation of low-level shallow clouds during the time of year when other cloud types are mostly absent. One component of ATOMIC was to characterize aerosol chemical, microphysical, optical, and cloud-nucleating properties to understand the impacts of aerosol on clouds and to improve the accuracy of model parameterizations of factors influencing the radiation budget of the northwest tropical Atlantic.

Based on sub-10 μm SAE and SSA, case study periods were identified to be representative of M, MDL, and MDBB aerosol. Marine aerosol had the highest sub-10 μm SSAs (0.97 ± 0.003) and low SAEs (-0.1 ± 0.05). MDL aerosol had slightly lower SSA values ranging from 0.88 to 0.95 and SAE values ranging from -0.15 to 0.06. MDBB aerosol, with varying amounts of the biomass burning component, had SSA values ranging, on average, from 0.82 to 0.92 and SAE values ranging from -0.05 to 0.45. Ångström Exponents derived from AOD measurements were more uniform (0.43–0.67) reflective of column-averaged values. Measurements of aerosol chemical composition provided confirmation of the designation of MDL and MDBB cases. The MDBB cases had higher supermicron ratios of $\text{nss K}^+/\text{Dust}$ and $\text{NO}_3^-/\text{Dust}$ than the MDL cases indicating a larger influence from biomass burning.

The presence of MDL or MDBB aerosol in the ATOMIC study region was modulated by the location of the North Atlantic subtropical high. During the MDL cases, the subtropical high was centered over the North Atlantic near 35°N and between 40° and 20°W . Back trajectories followed winds around the high at latitudes north of 15°N over the Sahara-Sahel dust corridor at altitudes primarily lower than 2 km. During the MDBB cases, the high was located further east over the Iberian Peninsula and north Africa. Back trajectories arrived from south of 15°N at altitudes above 1 km over the sub-Saharan region where agricultural burning is prevalent during winter. Measurements of vertical profiles of aerosol extinction confirmed the presence of aerosol layers aloft up to 2,500 m during the MDBB cases. During the M case, in the absence of a subtropical high, a high-pressure system over the southeast U.S. drew air from the Canadian Arctic to the ship.

One goal of ATOMIC was to assess the impact of aerosol on clouds and the region's radiation balance. Assuming a well-mixed boundary layer up to the lowest cloud base height, shipboard measurements can provide information on potential impacts of aerosol on low-level clouds. In addition, the stability of the lowest cloud base height of ~ 700 m (Figure 7) in the northwest tropical Atlantic allows for a direct comparison of CCN concentrations during different case study periods since MBL heights are uniform. Lowest CCN concentrations were measured during the M case due to a size distribution dominated by Aitken mode particles. Highest CCN concentrations were measured during the MDBB cases even though the volatile fraction of total CN and CCN was smallest corresponding to the presence of refractory particles at 230 °C. Accumulation mode

number concentrations were high with average concentrations during the case study periods ranging from 900 to 1,500 cm⁻³. In addition, average accumulation modal diameters were near calculated critical diameters for CCN activation.

The ATOMIC aerosol observations revealed the importance of the North Atlantic synoptic circulation in controlling the aerosol type transported to the northwest tropical Atlantic during wintertime. These results extend what has been previously reported for regions directly downwind of Africa across the North Atlantic basin to the Caribbean. The modulation of the subtropical high has a strong influence over the degree of biomass burning aerosol mixed with dust which affects CCN composition and concentrations. The lack of a strong subtropical high contributes to the dominance of marine aerosol in the ATOMIC region. The chemical, microphysical, optical, and cloud-nucleating properties for M, MDL, and MDBB aerosol reported here should prove useful for informing and validating model parameterizations of factors influencing the radiation budget of the northwest tropical Atlantic.

Data Availability Statement

All data are available at NOAA's National Center for Environmental Information (<https://www.ncei.noaa.gov/archive/accession/ATOMIC-2020>) and on the PMEL Atmospheric Chemistry data server (<https://saga.pmel.noaa.gov/data/>).

Acknowledgments

We thank the crew of the RV Ronald H. Brown for their enthusiastic help and cooperation throughout the ATOMIC cruise. We also thank Alton Daley (Caribbean Institute for Meteorology and Hydrology) and Wayne McGeary (Barbados Meteorological Services) for taking the AOD measurements. PMEL was funded by NOAA's Climate Program Office Climate Variability and Predictability Program. ILM was supported by the NOAA Climate and Global Change Postdoctoral Fellowship Program, administered by UCAR's Cooperative Programs for the Advancement of Earth System Science (CPAESS) under Award NA18NWS4620043B. PZ gratefully acknowledges support from the NOAA CVP program under Grant NA19OAR4310379. This is PMEL Contribution 5311.

References

- Adams, A. M., Prospero, J. M., & Zhang, C. (2012). CALIPSO-derived three-dimensional structure of aerosol over the Atlantic basin and adjacent continents. *Journal of Climate*, 25, 6862–6879. <https://doi.org/10.1175/jcli-d-11-00672.1>
- Anderson, T. L., & Ogren, J. A. (1998). Determining aerosol radiative properties using the TSI 3563 integrating nephelometer. *Aerosol Science & Technology*, 29, 57–69. <https://doi.org/10.1080/02786829808965551>
- Bates, T. S., Coffman, D. J., Covert, D. S., & Quinn, P. K. (2002). Regional marine boundary layer aerosol size distributions in the Indian, Atlantic and Pacific oceans: A comparison of INDOEX measurements with ACE-1 and ACE-2, and Aerosols99. *Journal of Geophysical Research*, 107(D19), 8026. <https://doi.org/10.1029/2001JD001174>
- Bates, T. S., Quinn, P. K., Coffman, D. J., Johnson, J. E., & Middlebrook, A. (2005). Dominance of organic aerosols in the marine boundary layer over the Gulf of Maine during NEAQS 2002 and their role in aerosol light scattering. *Journal of Geophysical Research*, 110, D18202. <https://doi.org/10.1029/2005JD005797>
- Bates, T. S., Quinn, P. K., Coffman, D. J., Schulz, K. S., Covert, D. S., Johnson, J. E., et al. (2008). Boundary layer aerosol chemistry during TexAQS/GoMACCS 2006: Insights into aerosol sources and transformation processes. *Journal of Geophysical Research*, 113, D00F01. <https://doi.org/10.1029/2008JD010023>
- Bates, T. S., Quinn, P. K., Frossard, A. A., Russell, L. M., Hakala, J., Petaja, T., et al. (2012). Measurements of ocean derived aerosol off the coast of California. *Journal of Geophysical Research*, 117, D00V15. <https://doi.org/10.1029/2012JD017588>
- Ben-Ami, Y., Koren, I., & Altaratz, O. (2009). Patterns of North African dust transport over the Atlantic: Winter vs. summer, based on CALIPSO first year data. *Atmospheric Chemistry and Physics*, 9, 7867–7875. <https://doi.org/10.5194/acp-9-7867-2009>
- Berner, A., Lurzer, C., Pohl, F., Preining, O., & Wagner, P. (1979). The size distribution of the urban aerosol in Vienna. *Science of the Total Environment*, 13, 245–261. [https://doi.org/10.1016/0048-9697\(79\)90105-0](https://doi.org/10.1016/0048-9697(79)90105-0)
- Birch, M. E., & Cary, R. A. (1996). Elemental carbon-based method for monitoring occupational exposures to particulate diesel exhaust. *Aerosol Science & Technology*, 25, 221–241. <https://doi.org/10.1080/02786829608965393>
- Bolton, D. (1980). The computation of equivalent potential temperature. *Monthly Weather Reviews*, 108, 1046–1053. [https://doi.org/10.1175/1520-0493\(1980\)108<1046:tcoept>2.0.co;2](https://doi.org/10.1175/1520-0493(1980)108<1046:tcoept>2.0.co;2)
- Bond, T., Anderson, T. L., & Campbell, D. (1999). Calibration and intercomparison of filter-based measurements of visible light absorption by aerosols. *Aerosol Science & Technology*, 30, 582–600. <https://doi.org/10.1080/027868299304435>
- Bony, S., Stevens, B., Frierson, D. M. W., Jakob, C., Kageyama, M., Pincus, R., et al. (2015). Clouds, circulation, and climate sensitivity. *Nature Geoscience*, 8, 261–268. <https://doi.org/10.1038/ngeo2398>
- Braaten, D. A., & Cahill, T. A. (1986). Size and composition of Asian dust transported to Hawaii. *Atmospheric Environment*, 20, 1105–1109. [https://doi.org/10.1016/0004-6981\(86\)90142-3](https://doi.org/10.1016/0004-6981(86)90142-3)
- Buck, N. J., Barrett, P. M., Morton, P. L., Landing, W. M., & Resing, J. A. (2021). Energy dispersive X-ray fluorescence methodology and analysis of suspended particulate matter in seawater for trace element compositions and an intercomparison with high-resolution inductively coupled plasma-mass spectrometry. *Limnology and Oceanography: Methods*, 19, 401–415. <https://doi.org/10.1002/lom3.10433>
- Burgos, M. A., Andrews, E., Titso, G., Alados-Arboledas, L., Baltensperger, U., Day, D., et al. (2019). A global view on the effect of water uptake on aerosol particle light scattering. *Scientific Data*, 6, 157. <https://doi.org/10.1038/s41597-019-0158-7>
- Carlson, T. N., & Prospero, J. M. (1972). The large-scale movement of Saharan air outbreaks over the northern equatorial Atlantic. *Journal of Applied Meteorology*, 11(2), 283–297. [https://doi.org/10.1175/1520-0450\(1972\)011<0283:tmsos>2.0.co;2](https://doi.org/10.1175/1520-0450(1972)011<0283:tmsos>2.0.co;2)
- CCCS. (2017). ERA5: Fifth generation of ECMWF atmospheric reanalyses of the global climate. Retrieved from <https://cds.climate.copernicus.eu/cdsapp#!/home>
- Chiappello, I., Moulin, C., & Prospero, J. M. (2005). Understanding the long-term variability of African dust transport across the Atlantic as recorded in both Barbados surface concentrations and large-scale total ozone mapping spectrometer (TOMS) optical thickness. *Journal of Geophysical Research*, 110, D18S10. <https://doi.org/10.1029/2004JD005132>
- Chouza, F., Reitebuch, O., Groß, S., Rahm, S., Freudenthaler, V., Toledano, C., & Weinzierl, B. (2015). Retrieval of aerosol backscatter and extinction from airborne coherent Doppler wind lidar measurements. *Atmospheric Measurement Techniques*, 8, 2909–2926. <https://doi.org/10.5194/amt-8-2909-2015>

- Cooke, W. F., Koffi, B., & Gregoire, J. (1996). Seasonality of vegetation fires in Africa from remote sensing data and application to a global chemistry model. *Journal of Geophysical Research*, 101, 21051–21065. <https://doi.org/10.1029/96JD01835>
- Doherty, O. M., Riemer, N., & Hameed, S. (2012). Control of Saharan mineral dust transport to Barbados in winter by the Intertropical Convergence Zone over West Africa. *Journal of Geophysical Research*, 117, D19117. <https://doi.org/10.1029/2012JD017767>
- Doherty, S. J., Quinn, P. K., Jefferson, A., Carrico, C. M., Anderson, T. L., & Hegg, D. A. (2005). A comparison and summary of aerosol optical properties as observed in situ from aircraft, ship, and land during ACE Asia. *Journal of Geophysical Research*, 110, D04201. <https://doi.org/10.1029/2004JD004964>
- Edwards, E.-L., Corral, A. F., Dadashazar, H., Barkley, A. E., Gaston, C. J., Zuidema, P., & Sorooshian, A. (2021). Impact of various air mass types on cloud condensation nuclei concentrations along coastal southeast Florida. *Atmospheric Environment*, 254, 118371. <https://doi.org/10.1016/j.atmosenv.2021.118371>
- Epsy, J. P. (1836). Essays on meteorology, No. IV: North east storms, volcanoes, and columnar clouds. *Journal of the Franklin Institute*, 22, 239–246.
- Evan, A. T., Heidinger, A. K., & Knippertz, P. (2006). Analysis of winter dust activity off the coast of West Africa using a new 24-year over-water advanced very high resolution radiometer satellite dust climatology. *Journal of Geophysical Research*, 111, D12210. <https://doi.org/10.1029/2005JD006336>
- Formenti, P., Elbert, W., Maenhaut, W., Haywood, J., & Andreae, M. O. (2003). Chemical composition of mineral dust aerosol during the Saharan Dust Experiment (SHADE) airborne campaign in the Cape Verde region, September 2000. *Journal of Geophysical Research*, 108(D18), 8576. <https://doi.org/10.1029/2002JD002648>
- Formenti, P., Rajot, J. L., Desboeufs, K., Caquineau, S., Chevaillier, S., Nava, S., et al. (2008). Regional variability of the composition of mineral dust from Western Africa: Results from the AMMA SOP0/DABEX and DODO field campaigns. *Journal of Geophysical Research*, 113, D00C13. <https://doi.org/10.1029/2008JD009903>
- Gaudichet, A., Echalar, F., Chatenot, B., Quisefit, J. P., Malingre, G., Cachier, H., et al. (1995). Trace elements in tropical African Savanna biomass-burning aerosols. *Journal of Atmospheric Chemistry*, 22, 19–39. <https://doi.org/10.1007/bf00708179>
- Glaser, G., Wernli, H., Kerkweg, A., & Teubler, F. (2015). The transatlantic dust transport from North Africa to the Americas—Its characteristics and source regions. *Journal of Geophysical Research: Atmospheres*, 120, 11,231–11,252. <https://doi.org/10.1002/2015JD023792>
- Hao, W. M., & Liu, M. (1994). Spatial and temporal distribution of tropical biomass burning. *Global Biogeochemical Cycles*, 8, 495–503. <https://doi.org/10.1029/94GB02086>
- Haywood, J., Francis, P., Osborne, S., Glew, M., Loeb, N., Highwood, E., et al. (2003). Radiative properties and direct radiative effect of Saharan dust measured by the C-130 aircraft during SHADE: 1. Solar spectrum. *Journal of Geophysical Research*, 108(D18), 8577. <https://doi.org/10.1029/2002JD002687>
- Holland, J. D. (1978). *The Chemistry of the atmosphere and oceans*. John Wiley.
- Huang, J., Zhang, C., & Prospero, J. M. (2010). African dust outbreaks: A satellite perspective of temporal and spatial variability over the tropical Atlantic Ocean. *Journal of Geophysical Research*, 115, D05202. <https://doi.org/10.1029/2009JD012516>
- Jahn, B.-M., Gallet, S., & Han, J. (2001). Geochemistry of the Xining, Xifeng and Jixian section, Loess Plateau of China: Eolian dust provenance and paleosol evolution during the last 140 k. *Chemical Geology*, 178, 71–94. [https://doi.org/10.1016/s0009-2541\(00\)00430-7](https://doi.org/10.1016/s0009-2541(00)00430-7)
- Johnson, B. T., Heese, B., McFarlane, S. A., Chazette, P., Jones, A., & Bellouin, N. (2008). Vertical distribution and radiative effects of mineral dust and biomass burning aerosol over West Africa during DABEX. *Journal of Geophysical Research*, 113, D00C12. <https://doi.org/10.1029/2008JD009848>
- Johnson, B. T., Osborne, S. R., Haywood, J., & Harrison, M. A. J. (2008). Aircraft measurements of biomass burning aerosol over West Africa during DABEX. *Journal of Geophysical Research*, 113, D00C06. <https://doi.org/10.1029/2007JD009451>
- Kahn, R. A., Anderson, J., Anderson, T. L., Bates, T. S., Brechtel, F., Carrico, C. M., et al. (2004). Environmental snapshots from ACE-Asia. *Journal of Geophysical Research*, 109, D19S14. <https://doi.org/10.1029/2003JD004339>
- Kaufman, Y. J., Koren, I., Remer, L. A., Tanre, D., Ginoux, P., & Fan, S. (2005). Dust transport and deposition observed from the Terra-Moderate resolution Imaging Spectroradiometer (MODIS) spacecraft over the Atlantic Ocean. *Journal of Geophysical Research*, 110, D10S12. <https://doi.org/10.1029/2003JD004436>
- Knippertz, P., Tesche, M., Heinold, B., Kandler, K., Toledano, C., & Esselborn, M. (2011). Dust mobilization and aerosol transport from West Africa to Cape Verde—A meteorological overview of SAMUM-2. *Tellus*, 63B, 430–447. <https://doi.org/10.1111/j.1600-0889.2011.00544.x>
- Knobelspiesse, K. D., Pietras, C., Fargion, G. S., Wang, M., Frouin, R., Miller, M. A., et al. (2004). Maritime aerosol optical thickness measured by handheld sun photometers. *Remote Sensing of Environment*, 93, 87–106. <https://doi.org/10.1016/j.rse.2004.06.018>
- Kramer, S. J., Alvarez, C., Barkley, A. E., Colarco, P. R., Custals, L., Delgado, R., et al. (2020). Apparent dust size discrepancy in aerosol reanalysis in North African dust after long-range transport. *Atmospheric Chemistry and Physics*, 20, 10047–10062. <https://doi.org/10.5194/acp-20-10047-2020>
- Lance, S., Medina, J., Smith, J. N., & Nenes, A. (2006). Mapping the operation of the DMT continuous flow CCN counter. *Aerosol Science & Technology*, 40, 242–254. <https://doi.org/10.1080/02786820500543290>
- Lewis, S. L., Salibas, G., Russell, L. M., Quinn, P. K., Bates, T. S., Aluwihare, L. I., & Behrenfeld, M. J. (2021). Seasonality of marine aerosol in the North Atlantic. *Frontiers*.
- Malm, W. C., Sisler, J. F., Huffman, D., Eldred, R. A., & Cahill, T. A. (1994). Spatial and seasonal trends in particle concentration and optical extinction in the United States. *Journal of Geophysical Research*, 99, 1347–1370. <https://doi.org/10.1029/93JD02916>
- McConnell, C. L., Highwood, E., Coe, H., Formenti, P., Anderson, B., Osborne, S., et al. (2008). Seasonal variations of the physical and optical characteristics of Saharan dust: Results from the dust outflow and deposition to the ocean (DODO) experiment. *Journal of Geophysical Research*, 113, D14S05. <https://doi.org/10.1029/2007JD009606>
- Moreno, T., Querol, X., Castillo, S., Alastuey, A., Cuevas, E., Herrmann, L., et al. (2006). Geochemical variations in aeolian mineral particles from the Sahara-Sahel dust corridor. *Chemosphere*, 65, 261–270. <https://doi.org/10.1016/j.chemosphere.2006.02.052>
- Moulin, C., Lambert, C., Dulac, F., & Dayan, D. (1997). Control of atmospheric export of dust from North Africa by the North Atlantic Oscillation. *Nature*, 387, 691–694. <https://doi.org/10.1038/42679>
- Nakamae, K., & Shiotani, M. (2013). Interannual variability in Saharan dust over the North Atlantic Ocean and its relation to meteorological fields during northern winter. *Atmospheric Research*, 122, 336–346. <https://doi.org/10.1016/j.atmosres.2012.09.012>
- NOAA. (2020). The Atlantic Tradewind Ocean-Atmosphere Mesoscale Interaction Campaign (ATOMIC), Barbados, 17 January–12 February 2020, NOAA NCEI [data set]. <https://www.ncei.noaa.gov/archive/accession/ATOMIC-2020>
- Omar, H., Winker, D. M., Vaughan, M. A., Hu, Y., Trepte, C. R., Ferrare, R. A., et al. (2009). The CALIPSO automated aerosol classification and lidar ratio selection algorithm. *Journal of Atmospheric and Oceanic Technology*, 26, 1994–2014. <https://doi.org/10.1175/2009JTECH1231.1>

- Osborne, S. R., Johnson, B. T., Haywood, J., Baran, A. J., Harrison, M. A. J., & McConnell, C. L. (2008). Physical and optical properties of mineral dust aerosol during the Dust and Biomass-burning Experiment. *Journal of Geophysical Research*, 112, D00C03. <https://doi.org/10.1029/2007JD009551>
- Pennypacker, S., & Wood, R. (2017). A case study in low aerosol number concentrations over the eastern North Atlantic: Implications for Pristine conditions in the remote marine boundary layer. *Journal of Geophysical Research: Atmospheres*, 122, 12393–12415. <https://doi.org/10.1002/2017JD027493>
- Perry, K., Cahill, T. A., Eldred, R. A., Dutcher, D. D., & Gill, T. E. (1997). Long-range transport of North African dust to the eastern United States. *Journal of Geophysical Research*, 102, 1225–1238. <https://doi.org/10.1029/97JD00260>
- Prospero, J. M., Bonatti, E., Schubert, C., & Carlson, T. N. (1970). Dust in the Caribbean atmosphere traced to an African dust storm. *Earth Planet Science Letters*, 9, 287–293. [https://doi.org/10.1016/0012-821X\(70\)90039-7](https://doi.org/10.1016/0012-821X(70)90039-7)
- Prospero, J. M., & Carlson, T. N. (1972). Vertical and areal distribution of Saharan dust over the Western equatorial North Atlantic Ocean. *Journal of Geophysical Research*, 77, 5255–5265. <https://doi.org/10.1029/JC077i027p05255>
- Prospero, J. M., & Lamb, P. J. (2003). African droughts and dust transport to the Caribbean: Climate change implications. *Science*, 302, 1024–1027. <https://doi.org/10.1126/science.1089915>
- Prospero, J. M., & Mayol-Bracero, O. L. (2013). Understanding the transport and impact of African dust on the Caribbean basin. *Bulletin of the American Meteorological Society*, 94, 1329–1337. <https://doi.org/10.1175/bams-d-12-00142.1>
- Prospero, J. M., & Nees, R. T. (1986). Impact of the North African drought and El Niño on mineral dust in the Barbados trade winds. *Nature*, 320, 725–738. <https://doi.org/10.1038/320735a0>
- Quinn, P. K., & Bates, T. S. (2005). Regional aerosol properties: Comparisons of boundary layer measurements from ACE 1, ACE 2, Aerosols99, INDOEX, ACE Asia, TARFOX, and NEAQS. *Journal of Geophysical Research*, 110, D14202. <https://doi.org/10.1029/2004JD004755>
- Quinn, P. K., Bates, T. S., Baynard, T., Clarke, A. D., Onasch, T. B., Wang, W., et al. (2005). Impact of particulate organic matter on the relative humidity dependence of light scattering: A simplified parameterization. *Geophysical Research Letters*, 32, L22809. <https://doi.org/10.1029/2005GL024322>
- Quinn, P. K., Bates, T. S., Coffman, D. J., Upchurch, L., Moore, R., Ziemba, L. D., et al. (2019). Seasonal variations in Western North Atlantic remote marine aerosol properties. *Journal of Geophysical Research: Atmospheres*, 124, 14240–14261. <https://doi.org/10.1029/2019JD031740>
- Quinn, P. K., Coffman, D. J., Bates, T. S., Miller, T. L., Johnson, J. E., Voss, K., et al. (2001). Dominant aerosol chemical components and their contribution to extinction during the Aerosols99 cruise across the Atlantic. *Journal of Geophysical Research*, 106, 20783–20809. <https://doi.org/10.1029/2000JD900577>
- Quinn, P. K., Coffman, D. J., Bates, T. S., Miller, T. L., Johnson, J. E., Welton, E. J., et al. (2002). Aerosol optical properties during INDOEX 1999: Means, variability, and controlling factors. *Journal of Geophysical Research*, 107(D19), 8020. <https://doi.org/10.1029/2000JD000037>
- Quinn, P. K., Coffman, D. J., Johnson, J. E., Upchurch, L. M., & Bates, T. S. (2017). Small fraction of marine cloud condensation nuclei made up of sea spray aerosol. *Nature Geoscience*, 10, 674–679. <https://doi.org/10.1038/ngeo3003>
- Quinn, P. K., Coffman, D. J., Kapustin, V. N., Bates, T. S., & Covert, D. S. (1998). Aerosol optical properties in the marine boundary layer during the first Aerosol Characterization Experiment (ACE-1) and the underlying chemical and physical aerosol properties. *Journal of Geophysical Research*, 103, 16743–16751. <https://doi.org/10.1029/97JD02345>
- Quinn, P. K., Thompson, E. J., Coffman, D. J., Baidar, S., Bariteau, L., Bates, T. S., et al. (2021). Measurements from the RV Ronald H. Brown and related platforms as part of the Atlantic Tradewind Ocean-Atmosphere Mesoscale Interaction Campaign (ATOMIC). *Earth System Science Data*, 13, 1759–1790. <https://doi.org/10.5194/essd-13-1759-2021>
- Roberts, G., & Nenes, A. (2005). A continuous-flow streamwise thermal gradient CCN chamber for atmospheric measurements. *Aerosol Science & Technology*, 39, 206–221. <https://doi.org/10.1080/027868290913988>
- Schepanski, K., Tegen, I., & Macke, A. (2009). Saharan dust transport and deposition towards the tropical northern Atlantic. *Atmospheric Chemistry and Physics*, 9, 1173–1189. <https://doi.org/10.5194/acp-9-1173-2009>
- Schroeder, P., Brewer, W. A., Choukulkar, A., Weickmann, A., Zucker, M., Holloway, M. W., & Sandberg, S. (2020). A compact, flexible, and robust micropulsed doppler lidar. *Journal of Atmospheric and Oceanic Technology*, 37, 1387–1402. <https://doi.org/10.1175/jtech-d-19-0142.1>
- Seinfeld, J. H. (1986). *Atmospheric chemistry and physics of air pollution* (p. 296). John Wiley.
- Shuster, G. L., Dubovik, O., & Holben, B. N. (2006). Angstrom exponent and bimodal aerosol size distributions. *Journal of Geophysical Research*, 111, D07207. <https://doi.org/10.1029/2005JD006328>
- Stein, A. F., Draxler, R. R., Rolph, G. D., Stunder, B. J. B., Cohen, M. D., & Ngan, F. (2015). NOAA's HYSPLIT atmospheric transport and dispersion modeling system. *Bulletin of the American Meteorological Society*, 96, 2059–2077. <https://doi.org/10.1175/bams-d-14-00110.1>
- Stephan, C., Schnitz, S., Schulz, H., Bellenger, H., Szoek, S. P. D., Acquistapace, C., et al. (2020) Ship- and island-based atmospheric soundings from the 2020 EUREC4A field campaign, AERIS. [Dataset]. <https://doi.org/10.25326/62,2020>
- Stevens, B., Bony, S., Farrell, D., Ament, F., Blyth, A., Fairall, C. W., et al. (2020) European project EUciding the RoIe of Cloud-Circulation Coupling in ClimAte (EUREC4A). [Dataset]. Earth System Science Data, in press. <https://doi.org/10.5194/essd-2021-18>
- Stevens, B., Farrell, D., Hirsch, L., Jansen, F., Nuijens, L., Serikov, I., et al. (2016). The Barbados cloud observatory: Anchoring investigations of clouds and circulation on the edge of the ITCZ. *Bulletin of the American Meteorological Society*, 97, 787–801. <https://doi.org/10.1175/BAMS-D-14-00247.1>
- Stratmann, F., & Wiedensohler, A. (1997). A new data inversion algorithm for DMPS measurements. *Journal of Aerosol Science*, 27, 339–340.
- Turpin, B. J., & Lim, H.-J. (2001). Species contributions to PM_{2.5} mass concentrations: Revisiting common assumptions for estimating organic mass. *Aerosol Science & Technology*, 35, 602–610. <https://doi.org/10.1080/02786820119445>
- Vial, J., Bony, S., Dufresne, J. L., & Roehrig, R. (2016). Coupling between lower-tropospheric convective mixing and low-level clouds: Physical mechanisms and dependence on convection scheme. *Journal of Advances in Modeling Earth Systems*, 8, 1892–1911. <https://doi.org/10.1002/2016MS000740>
- Wehner, B., Philippin, S., & Wiedensohler, A. (2002). Design and calibration of a thermodenuder with an improved heating unit to measure the size-dependent volatile fraction of aerosol particles. *Journal of Aerosol Science*, 33, 1087–1093. [https://doi.org/10.1016/s0021-8502\(02\)00056-3](https://doi.org/10.1016/s0021-8502(02)00056-3)
- Weinzierl, B., Ansmann, A., Prospero, J. M., Althausen, D., Benker, N., Chouza, F., et al. (2017). The Saharan aerosol long-range transport and aerosol-cloud-Interaction experiment: Overview and selected highlights. *Bulletin of the American Meteorological Society*, 98, 1427–1451. <https://doi.org/10.1175/bams-d-15-00142.1>
- Whittlestone, S., & Zahorowski, W. (1998). Baseline radon detectors for shipboard use: Development and deployment in the first aerosol Characterization experiment (ACE-1). *Journal of Geophysical Research*, 103, 16743–16751. <https://doi.org/10.1029/98JD00687>
- Wiedensohler, A., Orsini, D., Covert, D. S., Coffman, D. J., Cantrell, W., Havlicek, M., et al. (2007). Intercomparison study of the size-dependent counting efficiency of 26 condensation particle counters. *Aerosol Science & Technology*, 27, 224–242.

- Winklmeyer, W., Reischl, G. P., Lindner, A. O., & Berner, A. (1991). New electromobility spectrometer for the measurement of aerosol size distributions in the size range 1 to 1000 nm. *Journal of Aerosol Science*, 22, 289–296.
- Zuidema, P., Alvarez, C., Kramer, S. J., Custals, L., Izaquirre, M., Sealy, P., et al. (2019). Is summer African dust arriving earlier to Barbados? the updated long-term in situ dust mass concentration time series from Ragged point, Barbados, and Miami, Florida, *Bulletin of the American Meteorological Society*, 100, 1981–1986. <https://doi.org/10.1175/bams-d-18-0083.1>